

Integrated Study of X-ray Spectrum and Time Lags for HBL Mrk 421 within the Framework of the Multiple-Zone Leptonic Model

WEN HU (胡文)^{,1,2}, JIA-LAI KANG (康嘉来)^{,2,3}, ZHEN-YI CAI (蔡振翼)^{,2,3}, JUN-XIAN WANG (王俊贤)^{,2,3},
ZHEN-BO SU (苏镇波)^{,2,3} AND GUANG-CHENG XIAO (肖广成)¹

¹*Department of Physics, Jingtangshan University, Ji'an, 343009, P. R. China*

²*CAS Key Laboratory for Research in Galaxies and Cosmology, Department of Astronomy, University of Science and Technology of China, Hefei, Anhui 230026, P. R. China*

³*School of Astronomy and Space Science, University of Science and Technology of China, Hefei 230026, P. R. China*

ABSTRACT

We present the timing analysis of 10 archived XMM-Newton observations with an exposure of > 40 ks of Markarian 421. Mrk 421 is the brightest high-frequency-peaked BL Lac object (HBL) emitting in X-rays produced by electrons accelerated in the innermost regions of a relativistic jet pointing toward us. For each observation, we construct averaged X-ray spectra in 0.5–10 keV band, as well as 100 s binned light curves (LCs) in various subbands. During these observations, the source exhibited various intensity states differing by close to an order of magnitude in flux, with the fractional variability amplitude increasing with energy through the X-ray band. Bayesian power spectral density analysis reveals that the X-ray variability can be characterized by a colored noise, with an index ranging from ~ -1.9 to -3.0 . Moreover, both the standard cross-correlation function and cross-spectral methods indicate that the amount of time lags increases with the energy difference between two compared LCs. A time-dependent two-zone jet model is developed to extract physical information from the X-ray emission of Mrk 421. In the model, we assume that the jet emission mostly comprises a quasi-stationary component and a highly variable one. Our results show that the two-zone model can simultaneously provide a satisfactory description for both the X-ray spectra and time lags observed in different epochs, with the model parameters constrained in a fully acceptable interval. We suggest that shocks within the jets may be the primary energy dissipation process responsible for triggering the rapid variability, although magnetic reconnection cannot be excluded.

Keywords: BL Lacertae objects (158); X-ray astronomy (1810); Timing variation methods (1703); Shocks (2086)

1. INTRODUCTION

The highly non-thermal continuum emission from blazars is believed to originate from a relativistic jet, directed at a small angle ($\lesssim 10^\circ$) with respect to our line of sight (Urry & Padovani 1995). The broadband spectral energy distributions (SEDs) of blazars are characterized by a typical two-hump structure: a low-energy

(LE) hump that lies in the infrared to X-ray range and a high-energy (HE) hump that appears in the γ -rays ranging from MeV to TeV energies (Fossati et al. 1998; Abdo et al. 2010; Fan et al. 2016). BL Lacertae (BL Lac) objects are a subclass of blazars distinguished by their weakness or absence of broad emission lines in the optical band. Based on the peak frequency of the LE hump, BL Lacs are further subdivided into subclasses of high-, intermediate- and low-energy peaked BL Lac objects: HBLs, IBLs, LBLs, respectively. LBLs are defined to be objects with the LE hump in the IR-optical band, and HBLs as those with the LE hump peaking in the UV to the X-ray band. IBLs are distinguished by their LE hump peaking at optical to UV frequencies.

Corresponding author: Wen Hu
huwen.3000@jgsu.edu.cn

Corresponding author: Jun-Xian Wang
jxw@ustc.edu.cn

Another remarkable characteristic of blazars is the flux variation throughout the whole observable electromagnetic spectrum (i.e., from radio to very high-energy γ -rays) in diverse timescales ranging from a few minutes to years. The nature of the variability is similar to red noise, i.e., longer timescale variability has larger amplitude. Variations in flux are most dramatic and occur on timescales as short as a few hours or less at X-ray/TeV γ -ray energies (e.g., Ferrero et al. 2006; Abeysekara et al. 2017a; Yan et al. 2018; Noel et al. 2022; Devanand et al. 2022). Such rapid variability is commonly known as microvariability, intraday variability (IDV), or intranight variability, and is thought to be caused by the acceleration and radiative cooling of the emitting particles in the jets (e.g., Zhang 2002; Zhang et al. 2006; Böttcher & Baring 2019; Das & Chatterjee 2023).

It is commonly accepted that the LE hump is attributed to the synchrotron radiation produced by highly relativistic electrons/positrons in the blazar jet. The HE γ -rays hump is primarily interpreted as the inverse Compton (IC) scattering of the internal synchrotron photons (SSC; e.g., Bloom & Marscher 1996), or as the scattering of photons intercepting the jet from an external source (EC; e.g., Dermer et al. 2009), such as the accretion disk, the broad-line region, or the dusty/molecular torus. For BL Lacs, there is a relatively simple picture that most of the non-thermal emission from the jet can arise as the synchrotron and SSC radiation of relativistic electrons accelerated in a single blob of plasma which itself moves relativistically outward along the jet. In particular for HBL Mrk 421, the picture is strongly supported by the correlated X-ray/TeV flares and the roughly quadratic dependence of the X-ray and γ -ray fractional variability (e.g., Fossati et al. 2008; Aleksić et al. 2015; Baloković et al. 2016).

According to the simplified picture, various theoretical time-dependent and steady models have been developed (e.g., Mastichiadis & Kirk 1997; Kirk et al. 1998; Chiaberge & Ghisellini 1999; Kusunose et al. 2000; Li & Kusunose 2000; Böttcher & Chiang 2002; Finke et al. 2008; Zacharias & Schlickeiser 2013; Boula & Mastichiadis 2022). Such theoretical models have led to significant progress in our understanding of the jet physics and the underlying particle acceleration and cooling processes in HBLs. However, the conventional one-zone models are faced with a challenge posed by various variability and correlation studies (e.g., Fossati et al. 2000a,b; Brinkmann et al. 2005; Aharonian et al. 2009; Abeysekara et al. 2020; MAGIC Collaboration et al. 2021). One of the most peculiar aspects of blazar variability is the orphan flares detected in various blazars, e.g., orphan optical-UV flare observed in PKS 2155-304

(Wiercholska et al. 2019), orphan X-ray flare observed in S5 0716+714 (Rani et al. 2013), and orphan TeV γ -ray flare observed in B2 1215+30 (Abeysekara et al. 2017b). In these orphan events, the absence of correlated variability in other bands poses a serious issue for the single-zone SSC model, where the emission at various bands is thought to be radiated by the same population of relativistic electrons. Actually, there may be a need for two distinct zones to explain the observations (e.g., Tavecchio et al. 2011; MacDonald et al. 2015; Prince et al. 2019; Xue et al. 2019; Aguilar-Ruiz et al. 2022; Wang et al. 2022; Liu et al. 2023). In the scenario, one zone accounts for quiescent behavior, while another zone may be responsible for a detected outburst triggered by a localized energetic dissipation events such as magnetic reconnection (e.g., Giannios et al. 2009; Giannios 2013), shocks (e.g., Marscher & Gear 1985; Spada et al. 2001; Larionov et al. 2013), and MHD instabilities within the jet itself (e.g., Giannios & Spruit 2006; Nalewajko & Begelman 2012).

The optimal radiative window for exploring the variations in HBLs is X-ray, which is believed to be the synchrotron radiation arising from the high-energy tail of electrons accelerated in the innermost region of the jets. Characterizing the X-ray variability of HBLs is therefore important for exploring the physical nature of acceleration and cooling processes in blazar jets. A general property observed in HBLs is the "harder-when-brighter" behavior, which refers to a trend where an increase in flux is accompanied by a hardening of the spectrum as expected from a shift of the synchrotron peak to higher energies (e.g., Brinkmann et al. 2003; Ravasio et al. 2004; Abeysekara et al. 2017a; Gupta 2020; Chandra et al. 2021; Noel et al. 2022). Of particular interest is the formation of loops in the hardness ratio-intensity (HR-I) diagrams, which provides a model-independent diagnostic of the underlying physical process responsible for the observed emission. In theory, a clockwise loop in the HR-I diagram may indicate that the cooling process dominates the system, while an anti-clockwise loop may be caused by the acceleration process. The hysteresis of X-ray spectral variability can serve as an indication on whether the acceleration or the cooling process controls the observed variations.

Instead, the X-ray time delays measured between the soft-energy and hard-energy band variations, which are accompanied by the hysteresis loop, can allow us to deduce the underlying physical parameters for acceleration and radiation in the jet (Zhang et al. 2006; Das & Chatterjee 2023; Gokus et al. 2024). Particularly, the X-ray Fourier time lags could consistently provide stronger constraints and offer valuable insights into the underly-

Table 1. The Mrk 421 observations from the EPIC-pn on broad XMM-Newton.

Obs. ID	Date	MJD	PN mode	Exp.
	(yyyy-mm-dd)			ks
0099280301	2000-11-13	51861.93	SW-TK	46.6
0136540701	2002-11-14	52592.02	LW-TK	69.9
0136541001	2002-12-01	52609.97	TI-ME	69.9
0158970101	2003-06-01	52791.55	SW-TN	40.9
0150498701	2003-11-14	52957.69	TI-TN	47.7
0158971201	2004-05-06	53131.12	TI-ME	64.9
0158971301	2005-11-09	53683.78	TI-TN	58.7
0302180101	2006-04-29	53854.88	TI-TN	40.6
0411080301	2006-05-28	53883.09	SW-ME	68.4
0502030101	2008-05-07	54593.08	TI-TN	41.9

NOTE— SW, LW and TI stand for Small Window, Large Window and Timing science modes, respectively. TK, ME and TN stand for Thick, Median, and Thin filters, respectively.

ing mechanisms at work in the blazar jet (Zhang 2002; Kroon & Becker 2014; Finke & Becker 2014, 2015; Lewis et al. 2016).

In our work, the primary purpose is to explore the physics of blazar jets by modeling both the X-ray spectrum and the associated time lags. To quantitatively diagnose the cooling and acceleration behavior of the electrons responsible for the observed X-ray emission, both the cross-correlation function (CCF) and cross-spectral methods are employed to determine the time lags of variability in different X-ray bands. Then, we perform a detailed theoretical modeling of the time-dependent electron acceleration and radiation transport processes in the jets to extract the physical information contained in the X-ray emission. We focus our analysis on the IDV timescale X-ray variability of the famous HBL Mrk 421, using data taken from the public archives of XMM-Newton.

The paper is organized as follows. Section 2 gives the theoretical time lags resulting from the synchrotron cooling and Fermi acceleration mechanisms. In Section 3, we describe the archived XMM-Newton observations of Mrk 421, and data reduction, as well as the X-ray variability and time lags analysis of the public archival data. In Section 4, we present the theoretical model and the modeling results. A discussion follows in Section 5. Finally, we summarize the results in Section 6.

2. THEORETICAL PREDICTION

It is commonly accepted that the X-rays from blazars are attributed to the synchrotron emission of highly relativistic electrons in the jets. The observed soft lag be-

tween the soft $E_{s,\text{keV}}$ and high $E_{h,\text{keV}}$ energy band can be estimated from (e.g., Zhang 2002; Ravasio et al. 2004; Zhang et al. 2006; Devanand et al. 2022; Das & Chatterjee 2023)

$$\tau_s \simeq -53.7(1+z)^{\frac{1}{2}}\delta_D^{-\frac{1}{2}}B'^{-\frac{3}{2}}\Delta E \text{ min}, \quad (1)$$

where $\Delta E \equiv (E_{s,\text{keV}}^{-1/2} - E_{h,\text{keV}}^{-1/2})$, z is the source's redshift, B' is the magnetic field strength and δ_D is the Doppler factor of the emission region in the jet. In the derivation, $E_{s/h,\text{keV}}$ is the characteristic synchrotron energy of electrons with the Lorentz factor γ' . Note that the simple estimation of the time delay doubles that in Finke & Becker (2014) based on the analytical solution of the electron continuity equation using Fourier transformation method.

On the other hand, the acceleration process is not well understood yet and could operate in different ways. Particularly, diffusive shock acceleration is a widely discussed mechanism responsible for electron acceleration in the blazar jets. In the case of shock acceleration, the mean electron acceleration rate can be expressed as (see Lewis et al. 2016, and the references therein)

$$\dot{\gamma}'_{\text{sh}} = A_0^{\text{sh}}\gamma', \quad A_0^{\text{sh}} \equiv \frac{u_-^2}{c\ell_{\text{MHD}}\chi} \frac{\chi-1}{\chi+1} \quad (2)$$

where u_- is the upstream velocity measured in the frame of the shock, χ is the shock compression ratio, ℓ_{MHD} is the coherence length of the magnetohydrodynamic (MHD) waves.

The electrons may also experience stochastic acceleration due to resonant interactions with MHD turbulence. In the quasi-linear theory (e.g., Schlickeiser 1989; Becker et al. 2006), the MHD turbulence is described by a combination of Alfvén waves with different wave numbers. In the stochastic particle-wave interactions, the momentum diffusion coefficient of particles is determined by the wave-turbulence power spectrum as $W(k) \propto k^{-q}$, where k is the wavenumber. Here, we consider the hard-sphere turbulent spectrum (i.e., $q = 2$), leading to the acceleration timescale being independent of the electron energy. It favours the production of the brightest flares due to the most efficient re-acceleration of high-energy electrons. Moreover, the stochastic acceleration model can reasonably reproduce the broad-band blazar spectra (e.g., Katarzyński et al. 2006; Weidinger et al. 2010; Dmytriiev et al. 2021), in particular, very hard spectra (e.g., Stawarz & Petrosian 2008) and curved spectra (e.g., Tramacere et al. 2011). Such results suggest that the hard-sphere index may be supported in the blazar jet.

In the hard sphere approximation, the momentum diffusion coefficient can be phenomenologically described

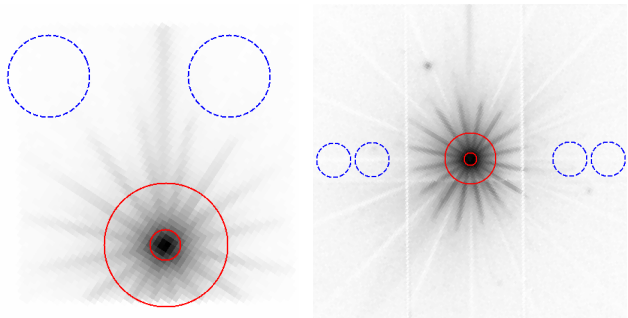


Figure 1. Examples of the source and background regions for SW (0099280301) and LW (0136540701) modes. The 0.5–10 keV images derived with *evselect* are plotted using *ds9*. The source regions, red annuli with inner radius of $15''$ and outer radius of $60''$, along with the background regions, blue circles (two for SW and four LW modes) with radius of $40''$, are over-plotted.

as

$$D_p(\gamma') = D_0 \gamma'^2, \quad (3)$$

for ultra-relativistic electrons. Then, the mean stochastic energy gain rate is given by

$$\dot{\gamma}'_{\text{sto}} = 4D_0 \gamma', \quad (4)$$

where $D_0 \propto s^{-1}$ is the momentum diffusion rate constant.

In either case, the hard lag is expected and the observed hard lag is predicted to be (Hu & Yan 2021)

$$\tau_h \simeq \frac{1+z}{\delta_D} t'_{\text{acc}} \Delta E, \quad (5)$$

where $\Delta E \equiv \ln(E_{h,\text{keV}}) - \ln(E_{s,\text{keV}})$, t'_{acc} is an energy-independent acceleration timescale. Assuming the synchrotron peak energy $E_{\text{pk,keV}}$ is determined by balancing the acceleration and synchrotron cooling, i.e., $t'_{\text{acc}} = t'_{\text{syn}}(E_{\text{pk,keV}})$, the expected lag can be expressed as

$$\tau_h \simeq 53.7(1+z)^{\frac{1}{2}} \delta_D^{-\frac{1}{2}} B'^{-\frac{3}{2}} E_{\text{pk,keV}}^{-1/2} \Delta E \text{ min.} \quad (6)$$

Note that the simple estimation is valid only for $E_{s,\text{keV}} < E_{h,\text{keV}} \lesssim E_{\text{pk,keV}}$.

Accordingly, the expected lags increase with increasing differences ΔE of the compared energy bands, and the signs of lags indicate whether the relativistic electrons responsible for the observed X-rays are dominated by the acceleration or cooling processes.

3. DATA ANALYSIS AND RESULTS

Mrk 421 is a prominent high-energy peaked blazar, with the synchrotron peak energy ranging from a fraction of a keV to several keV, even up to 10 keV (e.g., Tramacere et al. 2009; Ushio et al. 2010; Baloković et al.

2016). It is one of the closest and brightest blazars in the X-ray bands, at redshift $z = 0.031$. Because of its brightness, Mrk 421 has been studied in detail with XMM-Newton among other instruments (e.g., NuSTAR, Chandra and Suzaku). XMM-Newton with its high sensitivity, spectral resolving power and broad energy bandwidth, allows unprecedented time-resolved spectroscopy, uninterrupted by gaps because of a 48-hour-long orbital period (Jansen et al. 2001). It is therefore uniquely well-suited for studying IDV variability. In this work we focus on the European Photon Imaging Camera (EPIC) pn data (Strüder et al. 2001) of XMM-Newton to investigate the variability of Mrk 421, as it is more sensitive and less affected by photon pile-up effects.

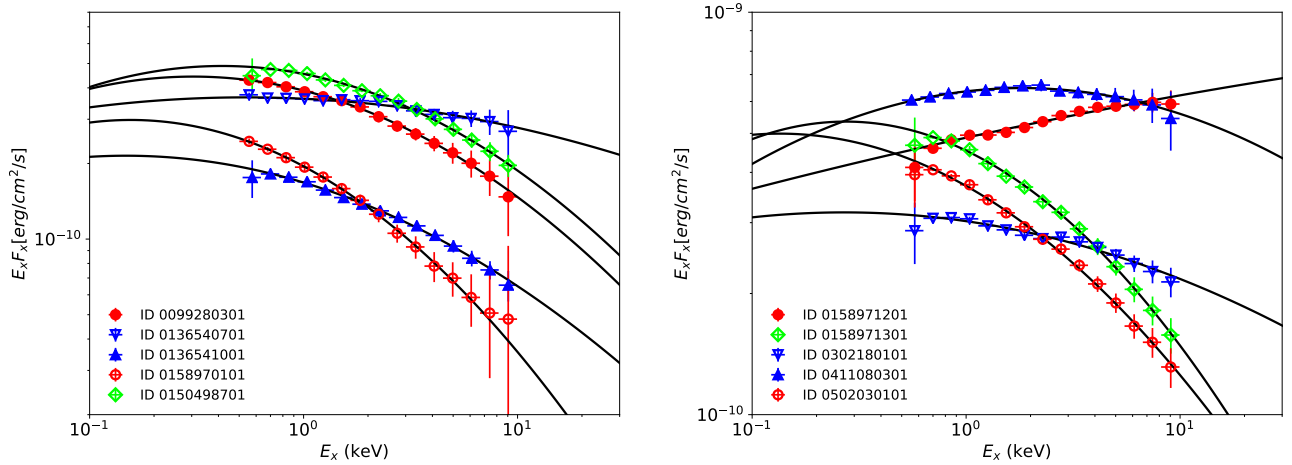
3.1. Data Selection and Reduction

So far, there are more than 150 archive XMM-Newton observations of Mrk 421. In order to perform high-quality timing analysis in a wide temporal frequency range, we search the XMM-Newton database for archival observations of Mrk 421 with an EPIC-pn exposure > 40 ks, and get a sample of 12 observations. Among them, two observations (Obs. IDs: 0099280101 and 0845000901) have multiple (two and three respectively) EPIC-pn exposures in different modes within a single observation. As none of these five individual exposures meets the > 40 ks criterion, we drop these two and obtain a sample of 10 observations, the detailed log of which is shown in Tab. 1. Note by coincidence, or due to unknown XMM strategy, all these observations were performed between 2002 and 2008. Among them, the pn camera was operated in Image mode for four and Timing mode for six observations.

Raw data are reduced using the latest XMM-Newton Science Analysis System (SAS, version 20.0.0) and the Current Calibration Files, following the standard pipeline in the XMM-Newton user guide. For data of Image mode, we firstly extracted the source light curves (LCs) and spectra within a circular region with a radius of $60''$, while extracting background from nearby source-free regions. However, using SAS task *epatplot*, we find serious pile-up effect in most observations. Therefore, we adopt annular regions to extract the source products, the inner radius being chosen to range from $15''$ and $25''$, depending on the severity of the pile-up effect. We present examples of how the source and background regions are adopted in Fig. 1. For data of Timing mode, we extract the source products with RAWX in [27:47], while background in [3:5], following the ‘‘XMM ABC

Table 2. The best-fitting log-parabolic model parameters and the fractional rms amplitude for 10 XMM-Newton observations.

Obs.ID	$E_p F_p$ 10^{-10} ergs/cm ² /s	E_p keV	b	$F_{\text{var}}(\%)$ (0.5–1) keV	$F_{\text{var}}(\%)$ (1–2) keV	$F_{\text{var}}(\%)$ (2–4) keV	$F_{\text{var}}(\%)$ (4–10) keV
0099280301	4.43 ± 0.17	0.30 ± 0.10	0.21 ± 0.05	2.55 ± 0.13	4.59 ± 0.13	8.98 ± 0.23	16.82 ± 0.36
0136540701	3.67 ± 0.05	0.54 ± 0.25	0.07 ± 0.03	13.64 ± 0.1	18.13 ± 0.1	24.26 ± 0.17	32.00 ± 0.25
0136541001	2.15 ± 0.17	0.15 ± 0.08	0.16 ± 0.04	3.41 ± 0.05	4.66 ± 0.06	6.14 ± 0.11	8.07 ± 0.21
0158970101	2.98 ± 0.46	0.16 ± 0.10	0.28 ± 0.08	6.15 ± 0.13	7.00 ± 0.18	8.68 ± 0.40	11.81 ± 0.99
0150498701	4.89 ± 0.09	0.42 ± 0.07	0.22 ± 0.03	7.96 ± 0.05	11.2 ± 0.06	16.19 ± 0.11	22.41 ± 0.19
0158971201	9.95 ± 0.47	$\gg 10$	0.01 ± 0.0	9.17 ± 0.04	13.8 ± 0.05	20.10 ± 0.08	27.87 ± 0.12
0158971301	5.35 ± 0.21	0.27 ± 0.07	0.23 ± 0.03	7.57 ± 0.04	9.17 ± 0.05	11.07 ± 0.09	13.70 ± 0.16
0302180101	3.18 ± 0.09	0.27 ± 0.16	0.07 ± 0.02	3.36 ± 0.04	4.82 ± 0.05	7.46 ± 0.09	11.80 ± 0.13
0411080301	6.48 ± 0.05	1.83 ± 0.19	0.12 ± 0.03	3.84 ± 0.07	5.05 ± 0.08	7.02 ± 0.14	10.70 ± 0.20
0502030101	4.99 ± 0.43	0.13 ± 0.07	0.17 ± 0.04	6.96 ± 0.04	8.34 ± 0.05	9.79 ± 0.10	11.38 ± 0.19


Figure 2. The X-ray spectrum of Mrk 421 measured in 10 observations. The solid black lines represent the best-fitting model obtained with a log-parabola function.

Guide”¹. Basically, no source-free region is available for the Timing mode observations where the PSF is larger than the field-of-view, and the background region is selected to minimize the contamination of the source (see Ng et al. 2010, for a detailed analysis). Such a small background region leads to small number of background counts (0.5–10 keV count rate ~ 0.2 cts/s), and thus biased estimation of the background level. However, since the source is very bright and the background only contributes to < 1 per cent within the source region, this bias should be negligible to the analysis in this work. We find no significant pile-up effect for the data of Timing mode. To study variability on a timescale of minutes, LCs, with a time bin of 100 s, are further reprocessed

with the task *epiclcorr*, applying corrections and background subtraction.

In Fig. 2, we present the unfolded X-ray spectrum within the 0.5–10 keV energy range, averaged over each of the 10 observations. The spectra are corrected for absorption with a neutral hydrogen column density fixed to the Galactic value of $N_{\text{H}} = 1.3 \times 10^{20}$ cm². To describe the X-ray spectral curvature of Mrk 421, a log-parabolic model has been used to fit the observed data:

$$E_x F_x = E_{pk} F_{pk} \left(\frac{E_x}{E_{pk}} \right)^{-b \log(E_x/E_{pk})} \quad (7)$$

where E_{pk} and $E_{pk} F_{pk}$ are the peak energy and flux, respectively, and b measures the spectral curvature around E_{pk} . All the spectra can be satisfactorily described by the model, with the best-fit parameters reported in Tab. 2. Note that the X-ray spectrum in Obs. ID 0158971201

¹ <https://heasarc.gsfc.nasa.gov/docs/xmm/abc/>

may be represented by a power law with a photon spectral index of ~ -1.9 .

We extracted the EPIC-pn LCs in two main energy bands, namely soft (0.5–2 keV) and hard (2–10 keV) X-rays, with the central energies being 1.25 and 6 keV, respectively. Additionally, we divided the soft X-ray band into two narrow bands: 0.5–1 keV and 1–2 keV, while the hard X-ray band was split into 2–4 keV and 4–10 keV. The corresponding central energies are 0.75, 1.5, 3 and 7 keV, respectively.

To quantify the strength of X-ray variability at different bands, we calculate the fractional root mean square (rms) variability amplitude F_{var} ². The uncertainty on F_{var} is calculated following the method described in [Vaughan et al. \(2003\)](#). We calculate F_{var} and its associated error $(F_{\text{var}})_{\text{err}}$ in all four narrow energy bands for the 10 observations. The results of the variability analysis are summarized in Tab. 2. It can be seen that during the 10 observations the source shows significant flux variation based on two conditions: $S^2 > \sigma_{\text{err}}^2$ and $F_{\text{var}} > 3 \times (F_{\text{var}})_{\text{err}}$ ([Dhiman et al. 2021](#); [Devanand et al. 2022](#)). Moreover, F_{var} tends to larger toward higher energy.

For illustration, the normalized LCs in the 1–2, 2–4 and 4–10 keV bands are shown in Fig. 8 in Appendix A. In the figure, we also show power spectral density (PSD) that is also often used to characterize the variability of blazar spectra. Due to limitations of observation durations, the PSDs are derived only within the range of approximately 10^{-5} to 5×10^{-3} Hz, and the PSDs are well described by a power-law component combined with a constant component. The spectral index of the PSD at lower frequencies falls within ~ 1.9 – 3 , indicating a rapid decrease in variability amplitude towards shorter timescales. On the other hand, the constant component at higher frequencies is attributed to uncertainties in the measured count rate, often referred to as white noise. Our findings demonstrate that the PSDs in the majority of observations are well above the white noise level up to $\sim 2 \times 10^{-4}$ – 10^{-3} Hz, which corresponds to variability timescales on hour to sub-hour timescales. Notably, in special cases (e.g., Obs. ID 0502030101), the variability is still present, reaching frequencies of $\sim (2 - 3) \times 10^{-3}$ Hz, which translates to timescales shorter than 10 minutes.

² The fractional rms variability amplitude is defined as $F_{\text{var}} = \sqrt{\sigma_{\text{XS}}^2 / \bar{x}^2}$, with $\sigma_{\text{XS}}^2 = S^2 - \sigma_{\text{err}}^2$ and \bar{x} being the excess variance and the arithmetic mean of a light curve x_j , respectively. Here, the sample variance and mean square error are $S^2 = \frac{1}{N-1} \sum_{j=1}^N (x_j - \bar{x})^2$ and $\sigma_{\text{err}}^2 = \frac{1}{N} \sum_{j=1}^N \sigma_{\text{err},j}^2$, respectively.

In the following analysis, we investigate the time delays associated with the interband variability in different X-ray energy bands. To maximize the utility of the available data, the interband time delays include time lags for 4–10 keV with respect to 0.5–1, 1–2, 0.5–2 and 2–4 keV, delays for 2–4 keV with respect to 0.5–1, 1–2, and 0.5–2 keV, as well as delays for 2–10 keV with respect to 0.5–1, 1–2, and 0.5–2 keV, and delays between 0.5–1 and 1–2 keV. To comprehensively assess the possible time delays between the low- and high-energy variations, we employ two distinct techniques: the cross-correlation function (CCF) method in the time domain and the cross-spectral method in the frequency domain.

3.2. Cross-correlation analysis in the time domain

The lags between different X-ray bands are calculated using the popular interpolated cross-correlation functions (CCFs) method described in [Peterson et al. \(1998\)](#). As suggested in the previous works (e.g., [Peterson et al. 1998](#); [Zhang et al. 2006](#)), the centroid of the CCF τ_{cent} is used to quantify the time lags between two highly variable LCs, representing the intrinsic complexities of the underlying variability processes. The primary reason is that τ_{cent} may account for the CCF asymmetries that are usually seen in AGN variability. Uncertainties on the lags are estimated using the flux randomization and random subset selection (FR/RSS) simulation. To estimate the uncertainties, the distribution of the CCF centroid is built up based on all points with correlation coefficients in excess of 80% of the CCF peak value (i.e., the maximum correlation coefficient). The calculations were done using a publicly available code *PyMCCF*³. For each pair of LCs, the time lag τ and its uncertainty σ are estimated by fitting a Gaussian model to the cross-correlation centroid distribution (CCCD), and the weighted average $\langle \tau_c \rangle$ of these values is computed⁴. The results are shown in Fig. 3. For illustrative purposes, the CCCDs from the selected 10 observations are shown in Fig. 9 in Appendix B.

In Fig. 3, we display the CCF lags computed from the original LCs as a function of the differences ΔE of the compared energy bands, with $\Delta E \equiv E_{\text{s,keV}}^{-1/2} - E_{\text{h,keV}}^{-1/2}$ for $\langle \tau_c \rangle < 0$, and $\Delta E \equiv \ln(E_{\text{h,keV}}) - \ln(E_{\text{s,keV}})$ otherwise. For comparison, we also show the measured lags in several previous works, where the time lags are estimated with different techniques: (1) fitting the CCF with an asymmetric Gaussian profile to find the peak

³ https://bitbucket.org/oknyansky/python_mccf/src/master/

⁴ To the lag τ obtained for each pair of LCs, we assigned as weight $1/\sigma^2$, where σ represents 68% confidence limits around the lag corresponding to the peak of the Gaussian function.

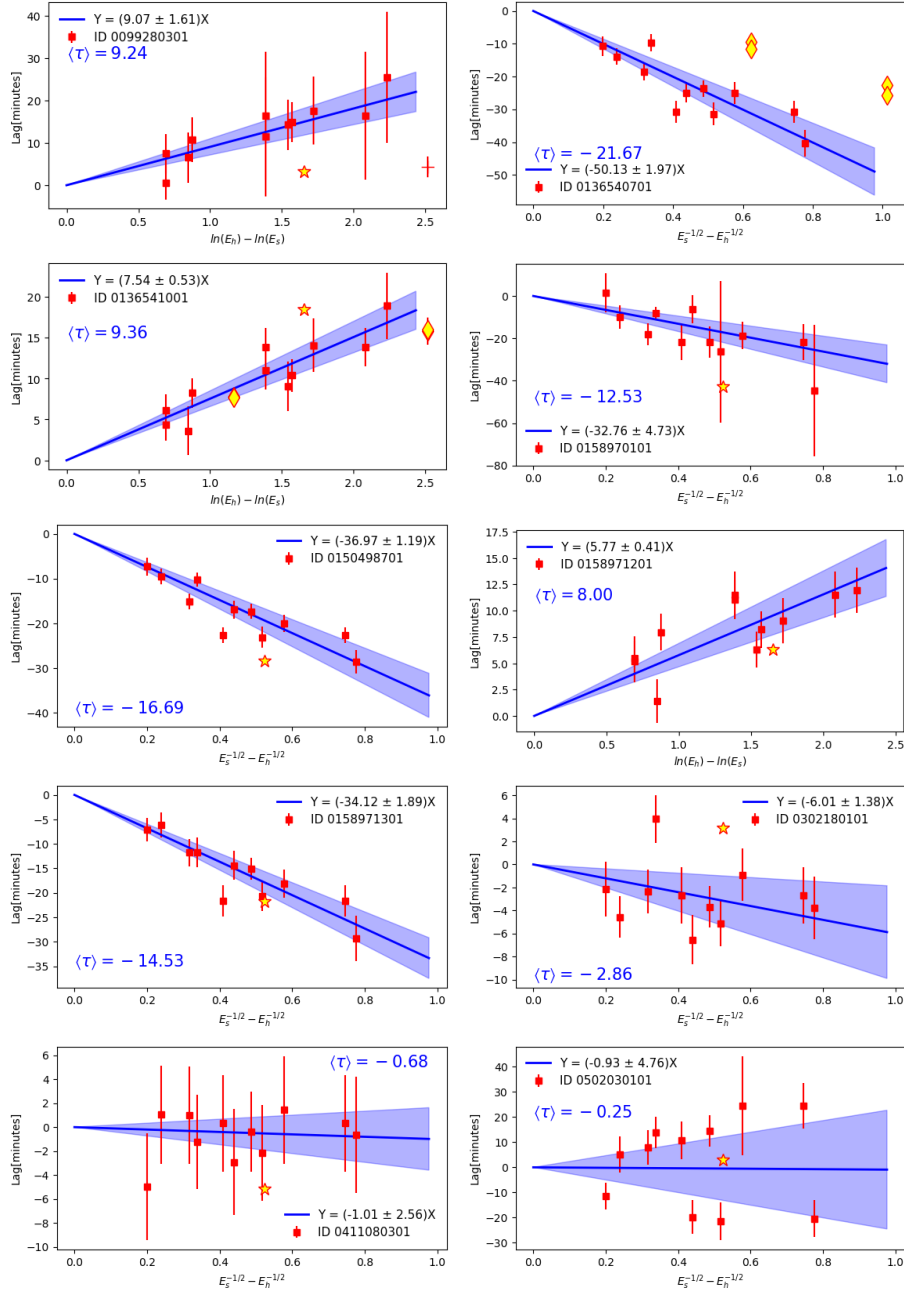


Figure 3. The CCF time lags as a function of the energy differences ΔE . Which ΔE is used depends on whether the weighted mean lag is negative or positive lag. A linear function is fitted to each of the trends, and the uncertainty region is shaded in blue. The stars denote the results from Noel et al. (2022). The diamonds in Obs. ID 0136540701 and 0136541001 denote the results from Ravasio et al. (2004). For Obs. ID 0099280301, the lag reported in Brinkmann et al. (2003) is denoted by the symbol ‘+’.

position (Brinkmann et al. 2003; Ravasio et al. 2004); (2) fitting the central peak of the Discrete correlation function (DCF) with a Gaussian function and taking the peak position of the function as the delay value (Noel et al. 2022).

It is clear from Fig.3 that in the first eight observations the interband time lags exhibit a systemic trend, i.e., the amount of lag $|\tau_c|$ tend to become larger with increasing cross-correlated energy difference ΔE . For each case, linear regression analysis of the scatter plot indicates that the $\tau_c - \Delta E$ trend can be adequately described by the expected linear relation, and most of the data points are within 95% confidence ranges. Among the eight observations, there are three cases exhibiting the systematic hard lag and five cases exhibiting the systematic soft lag. Except for Obs. ID 0302180101, the time lags predicted in the $\tau_c - \Delta E$ trends are compatible with previous results measured with different techniques. Based on the DCF maximum fitting, a minor hard lag of ~ 3 minutes between the 0.3–2.0 keV and 2.0–10 keV X-ray bands was reported in Noel et al. (2022) for Obs. ID 0302180101⁵. On the contrary, there may exist a clear soft-lag trend in the scatter plot of $\tau_c - \Delta E$, although a slight hard lag of 4.0 ± 2.0 minutes may be present between 0.5–1 and 1–2 keV bands, and this measurement lies outside the 95% confidence intervals of the best fitting. Using the best-fit relation for $\tau_c - \Delta E$ trend, a soft lag of ~ 3 minutes between 0.3–2 and 2–10 keV bands can be predicted. However, it is worth noting that any time lags comparable to or less than bin size (100 s) adopted should be taken with caution.

In the last two observations: Obs. IDs 0411080301 and 0502030101, there are no systematic trends. In Obs. ID 0411080301, no evidence for time leads or lags is present. Our results show that almost all of the lags are consistent with zero lag within the 1σ intervals. Moreover, we notice no clear trend in the plot of $\tau - \Delta E$, where the best-fitting slope is statistically consistent with zero within 95% confidence intervals. As claimed by previous works (e.g., Ravasio et al. 2004; Ferrero et al. 2006; Noel et al. 2022), absence of a non-zero time lag may be due to a superposition of the various lags in individual features. In Obs. ID 0502030101, one can see both the significant positive and negative lags. The results show that the flux variation at the 4-10 keV reference band leads those at the other four

lower energy bands, whereas the remaining 7 pairs of LCs exhibit clear hard lags. Throughout the observation, XMM-Newton may sample only a decaying phase of a possible major flare (see Fig.8). The presence of non-zero lag may be mainly caused by the differences in the decay slopes of the compared LCs, producing, on average, soft lags or hard lags (see detailed discussion in Ravasio et al. 2004). Actually, previous work showed a minor hard lag between 0.3–2 keV and 2–10 keV, with the variation of soft photons preceding that of hard photons by 0.17 ks. It appears to be compatible with the lag predicted by our best-fit relation.

It is worth noting that the CCF time lags measured from the structured or asymmetrical LCs as a whole may roughly represent a weighted average value combining the delays of the various substructures or an index of the LC asymmetry (Ravasio et al. 2004). Thus, one should perform a careful check of the behaviour of the single subcomponent before using the results to test the blazar models. However, it is a tedious task to check the results based on the CCF techniques (e.g., Brinkmann et al. 2003; Ravasio et al. 2004; Brinkmann et al. 2005). An alternative approach for checking and measuring the lags is based on Fourier techniques, which can provide the frequency-dependent time lag of the average cross-power spectrum between two different time series. The cross-spectral method may be superior to the commonly used CCF method for measuring the time lag from the complex or irregular LCs (Zhang 2002).

3.3. Cross-spectral analysis in the frequency domain

In the section, we present the analysis of the X-ray time lags in the Fourier domain. We calculate the frequency-resolved time lags using a standard Fourier approach reviewed in detail by Uttley et al. (2014). Briefly, estimation of the lag consists of three major steps. Firstly, LCs are split into segments of identical length in two bands, and the periodograms and cross-spectrum are calculated using the DFT for each segment of the resulting LCs (see Appendix C). To reduce the effects of noise, the periodograms and the cross-spectrum are then averaged over Fourier frequencies in a given frequency bin centered at ν_f , as well as over the number of segments, allowing the raw coherence to be calculated from the binned periodograms and cross-spectrum (Vaughan & Nowak 1997). Finally, one measures the phase lags from the argument of the cross-spectrum in each bin and divides them by $2\pi\nu_f$ to give a lag-frequency spectrum between a pair of LCs at two bands, and their uncertainties are given by the coher-

⁵ In the work, a positive value for the lag means that the soft channel signal is delayed with respect to the hard signal, and it is known as a soft lag. Conversely, a negative value indicates a hard lag, with the hard channel signal lagging behind the soft signal.

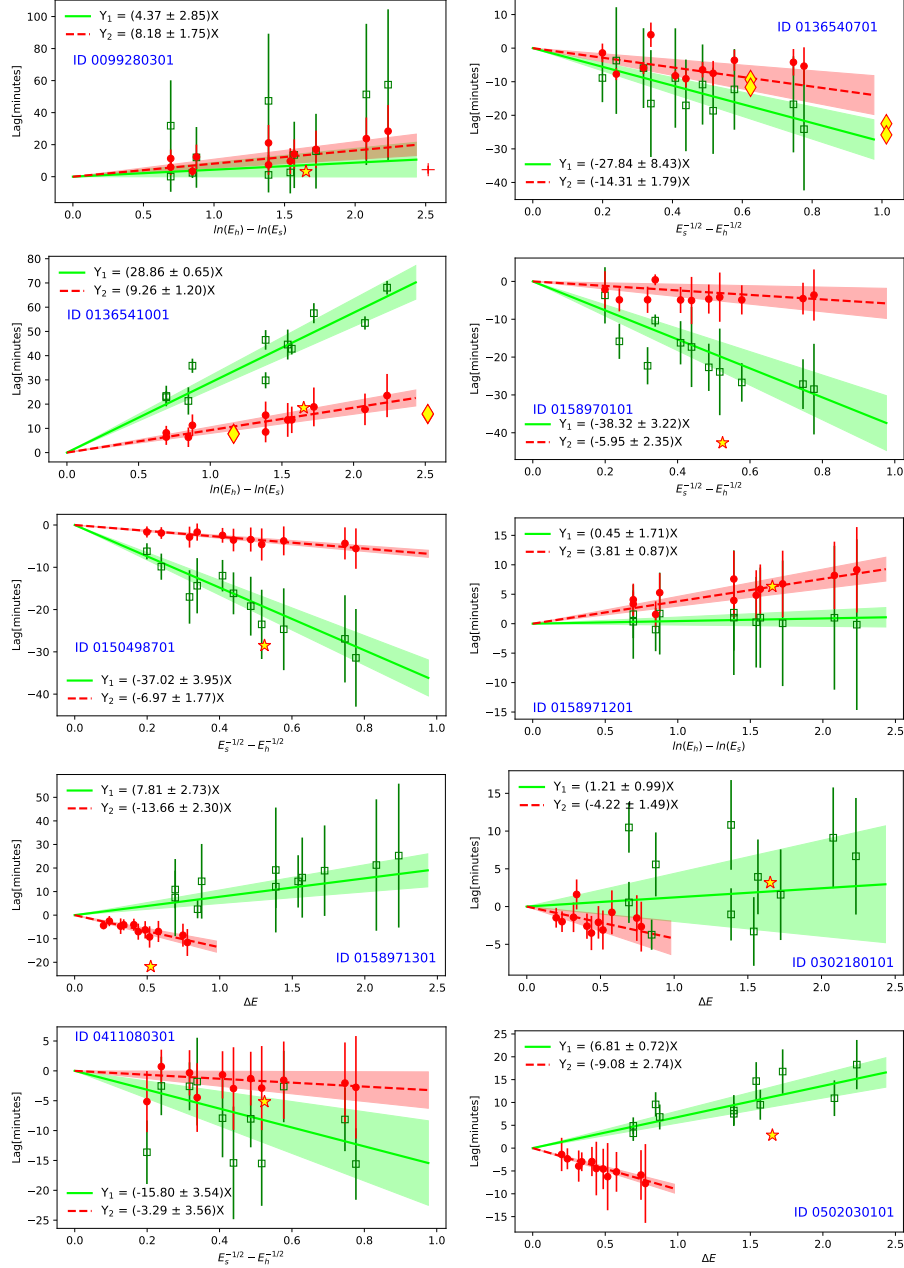


Figure 4. The lowest-frequency time lags as a function of the differences ΔE . The open green squares denotes the lowest-frequency lag in τ_1 , and the filled red circles denotes the lowest-frequency lag in τ_2 .

ence in each frequency bin. The procedure was carried out using the X-ray timing analysis package *pyLag*⁶.

For each pair of LCs, we obtain the lag-frequency spectra in five logarithmically spaced bins, ranging from the lowest frequency T^{-1} (where T is the time duration of each observation) to the Nyquist frequency of 5×10^{-3} Hz. The resulting lag-frequency spectra are denoted as

τ_1 . To explore the variability at different timescales in more detail, we then divide each LC into two segments of equal duration and recalculate the lag-frequency spectra, referred to as τ_2 . The minimum frequency bin in τ_2 is about twice that in τ_1 . It helps us to reveal the potential profile of the lag-frequency spectra. The results reveal that, for most observations, lags predominantly appear in the low Fourier-frequency bin, where the color noise dominates (see Appendix A). We show the resulting lags at the lowest frequencies in τ_1 and τ_2 in Fig.4, as

⁶ <http://github.com/wilkinsdr/pylag>

denoted by the green open squares and red filled circles, respectively. To show the dependence of the lags on the frequency, the lag-frequency spectra for 0.5–2 keV/1–2 keV bands, with respect to 2–10 keV band, are plotted in Fig. 6, as denoted by the red and green symbols, respectively. Moreover, a direct comparison of the CCF lags with the Fourier time lags is also shown in the figure. It is clear that the CCF lags in different epochs are in good qualitative agreement with the Fourier lags at the lowest frequency bin in τ_1 or τ_2 .

Similar to the results quantified with the CCF method, the lowest-frequency Fourier lags in the plot of $\tau - \Delta E$ follow the expected linear relation. The results further confirm the presence of hard lags, as measured by the CCF method in Obs. IDs 0099280301, 0136541001 and 0158971201, along with soft lags in Obs. IDs 0136540701, 0158970101 and 0150498701. Comparing the lags measured by two different methods, we note that the lowest-frequency hard lags in τ_2 are more closely aligned with the CCF lags compared to those in τ_1 . Conversely, the lowest-frequency soft lags in τ_1 are more consistent with the CCF lags than those in τ_2 .

For Obs. IDs 0158971301, 0302180101 and 0502030101, the cross-spectral analyses indicate that the lowest-frequency lags in τ_2 exhibit systematic soft lags, while those in τ_1 exhibit an opposite trend. In Obs. ID 0158971301, the lowest-frequency soft lags in τ_2 are comparable with the lags measured using CCF method, while those in τ_1 exhibit a systematic hard-lag trend, although these results are associated with large errors. In Obs. ID 0302180101, the lowest-frequency lags in τ_1 are highly scattered, and no clear trend can be observed. However, the lag between 0.3 – 2 and 2 – 10 keV band predicted by the best-fit result is in good qualitative agreement with that estimated in Noel et al. (2022).

For Obs. ID 0411080301, all points in the plot of $\tau - \Delta E$ are consistent with zero lags, which is in agreement with the measured CCF lags. However, it seems that a soft-lag trend may exist.

4. MODEL DESCRIPTION

Generally, the non-thermal emission of blazars is thought to be the combination of radiation from various regions of the jets with electron spectra at different stages of evolution (e.g., Blandford & Königl 1979; Königl 1981). Given the X-ray observations of Mrk 421, the LCs in most epochs can be characterized by long-term trends lasting for time scales comparable to or longer than the observations' length, with superimposed small features occurring on short timescales of hours or even a few minutes. This may suggest that more than one emission region may be in operation in the system

(Brinkmann et al. 2005). Since we mainly focus on the X-ray radiation emerging from the innermost regions of the jets, we employ the simplest version of a multi-zone jet model to investigate the jet's physical properties contained in the broadband X-ray spectrum and the inter-band time lags measured in different epochs. In the model, the blazar emission predominantly consists of a quasi-stationary component that changes only on long timescales and a non-stationary component responsible for short-timescale variability.

For convenience, the compact dissipation zone responsible for the rapid variation is usually treated as a spherical blob of size R' containing a randomly tangled magnetic field of strength B' . As it propagates outward along the jet, a population of ultra-relativistic electrons (and positrons) is injected uniformly throughout the blob. The injected electrons experience further acceleration due to interactions with shocks or MHD waves, and radiative losses until they escape from the blob. The most important radiation mechanisms for electrons are synchrotron and SSC radiation. Due to the relativistic beaming effects, the intrinsic radiation produced in the comoving frame of the blob is Doppler boosted by a factor of δ_D^4 in the observer's frame, while the variability timescale is reduced by a factor of δ_D^{-1} . Then, rapid variability can be observed.

The quasi-stationary emission may arise from an extended inhomogeneous or stratified region responsible for generating X-ray emission. For the modeling of the quasi-stationary emission, we simplify the spatial geometry as a spherical plasmoid with different physical properties including the magnetic field strength, Doppler factor, spatial size, and the emitting electrons. Thus, the blob may represent an average over the entire region. To facilitate parameter comparison between different epochs, the quasi-stationary emission remains constant and is treated as the background emission.

In the model, the population of the injected electrons is assumed to be provided by a significantly smaller co-spatial non-radiative acceleration region, where seed electrons undergo significant energization by shocks (e.g., Kirk et al. 1998; Böttcher & Baring 2019; Chandra et al. 2021) or magnetic reconnection events (e.g., Sironi & Spitkovsky 2014; Sironi et al. 2015), but contribute only a negligible amount of radiation due to a low magnetic field. Thus, it is reasonable to consider that the injected electrons exhibit a time-dependent nature. For simplicity, we assume that the time-dependent injection process of the energetic electrons is described by the time-dependent function $Q'_e(\gamma', t')$, which can be decoupled into the product of $f'_e(t)$ and $q'_e(\gamma')$, with $f'_e(t')$

and $q'_e(\gamma')$ being the time-dependent profile and time-independent energy distribution, respectively.

In these two zones, we assume that the electron injection spectrum $q'_e(\gamma')$ follows the same power-law distribution form characterized by four parameters: the normalization constant q'_0 , the minimum $\gamma'_{i,\min}$ and maximum $\gamma'_{i,\max}$ Lorentz factors and the power-law index p , represented by: $q'_e(\gamma', t') = q'_0 \gamma'^{-p} H(\gamma'; \gamma'_{i,\min}, \gamma'_{i,\max})$, where $H(\cdot)$ is the Heaviside function defined by $H = 1$ if $\gamma'_{i,\min} \leq \gamma' \leq \gamma'_{i,\max}$ and $H = 0$ otherwise.

4.1. Electron Transport Equation

For simplicity, we assume that the two components are decoupled from each other. Then, the evolution of the emitting electron distribution (EED) in both zones can be independently described by the transport equation (e.g. Schlickeiser 1984; Stawarz & Petrosian 2008; Diltz & Böttcher 2014; Hu et al. 2023)

$$\begin{aligned} \frac{\partial N'_e(\gamma', t')}{\partial t'} &= \frac{\partial}{\partial \gamma'} \left\{ \gamma'^2 D_p(\gamma') \frac{\partial}{\partial \gamma'} \left[\frac{N'_e(\gamma', t')}{\gamma'^2} \right] \right\} \\ &\quad - \frac{\partial}{\partial \gamma'} [(A_0^{\text{sh}} \gamma' + \dot{\gamma}'_{\text{rad}}) N'_e(\gamma', t')] \\ &\quad - \frac{N'_e(\gamma', t')}{t'_{\text{esc}}} + Q'_e(\gamma', t'). \end{aligned} \quad (8)$$

where $D_p(\gamma')$ is the momentum diffusion coefficient for interactions with MHD waves, A_0^{sh} accounts for first-order Fermi acceleration used in Eq. 2, and t'_{esc} is the escape timescale which describes spatial transport of the electrons in the blob. The term $\dot{\gamma}'_{\text{rad}}$ represents the radiative losses due to synchrotron and SSC processes, and is calculated using standard formulas in the literatures (e.g., Jones 1968; Moderski et al. 2005; Finke et al. 2008).

In brief, we assume that the observed X-ray and TeV γ -rays are the sum of two standard blobs that radiate simultaneously and characterized by different physical conditions. For each zone, there are at least 10 physical quantities, i.e., B' , δ_D , R' , A_0^{sh} , D_0 , t'_{esc} , q'_0 , $\gamma'_{i,\min}$, $\gamma'_{i,\max}$ and p . Among those, the first three quantities describe the global properties of the zone, while the injection electron spectrum is described by the last four quantities. The quantities A_0^{sh} , D_0 and t'_{esc} determine the acceleration and escape of the injected electrons. The EED can be obtained by solving the diffusion equation numerically, and the expected synchrotron and SSC radiation can be calculated following the methods described in the literatures (e.g., Rybicki & Lightman 1979; Crusius & Schlickeiser 1986; Finke et al. 2008; Deng et al. 2021).

To explore the parameter space more effectively, we use the observed synchrotron peak frequency ν_{pk} and electron escape efficiency η_{esc} as the input parameters

instead of D_0 and t'_{esc} . Since the peak Lorentz factor γ'_{pk} corresponding to ν_{pk} is approximately equal to the equilibrium Lorentz factor γ'_{eq} determined by the balance of the synchrotron cooling and acceleration, the energy-independent acceleration timescale t'_{acc} can be evaluated by the relationship (Hu & Yan 2021)

$$t'_{\text{acc}} = \frac{6\pi m_e c}{\sigma_T B'^{3/2}} \sqrt{\frac{\nu_0 \delta_D}{\nu_{\text{pk}}(1+z)}}, \quad (9)$$

where $\nu_0 = 4m_e c^2 / 3h B_{\text{cr}}(1+z)$, with m_e , c , h and B_{cr} being the rest mass of electrons, light speed, Planck's constant and critical magnetic field strength, respectively.

Then, the momentum diffusion coefficient can be deduced through the following relationship:

$$D_0 = \frac{1}{(4 + a_{\text{sh}})t'_{\text{acc}}} \quad (10)$$

where $a_{\text{sh}} \equiv A_0^{\text{sh}}/D_0$. In particular, we assume that stochastic acceleration plays a dominant role in energization of the injected electrons. This is motivated by the observations that the X-ray spectral shape of Mrk 421 is better represented by a log-parabola model rather than by a single power law or broken power-law models (e.g., Brinkmann et al. 2003; Rivasio et al. 2004), and the curvature parameter decreases as the synchrotron peak energy increases (e.g., Tramacere et al. 2007). Without loss of generality, we set $a_{\text{sh}} = 0$ in our modelling.

On the other hand, the escape timescale associated with spatial diffusion can be written as $t'_{\text{esc}} = t'_{\text{acc}}/\eta_{\text{esc}}$, using the well-known relation between the momentum and spatial diffusion coefficient given by $D_p(\gamma')D_x(\gamma') \simeq \gamma'^2 \beta_A^2 c^2/9$ with β_A denoting the dimensionless Alfvén velocity.

The full time-dependent and steady-state EED are computed numerically by solving Eq. (8). The implicit Crank-Nicolson scheme is used to numerically solve the transport equations. We tested our numerical code with the analytical solution for the steady-state and time-dependent EED in Appendix D.

4.2. Modeling the X-ray and TeV γ -ray background emission

For a better understanding of the observed X-ray spectrum and time lags in different epochs, we first need to model the quasi-stationary background emission from the jet that generates the synchrotron X-rays and TeV γ -rays emitted via the SSC process.

Abdo et al. (2011) and Baloković et al. (2016) organized two coordinated MWL observations of Mrk 421

Table 3. Input model parameters and derived quantities for the simultaneous SEDs collected in 2009 and 2013 MWL campaigns.

MWL camps	δ_D	B'	R'	$\nu_{\text{pk}}(E_{\text{pk}})$	q'_0	$\gamma'_{i,\text{min}}$	$\gamma'_{i,\text{max}}$	p	η_{esc}	t'_{acc}	D_0	U'_e/U'_B
		G	10^{15}cm	10^{17}Hz (keV)	s^{-1}	10^3	10^5			R'/c	10^{-6}s^{-1}	
(1)	(2)	(3)	(4)	(5)	(6)	(7)	(8)	(9)	(10)	(11)	(12)	(13)
2009	27	0.08	12.0	2.5(1.03)	4.03×10^{47}	2.0	35.0	2.5	1.26	1.69	0.37	8.6
2013	25	0.1	18.5	0.5(0.21)	2.38×10^{48}	2.0	12.0	2.7	1.26	1.69	0.24	2.0

NOTE—Column(1): Multi-wavelength campaigns. Column (2): The Doppler factor. Column (3): The magnetic field strength. Column (4): The synchrotron peak frequency (in units of keV). Column (5): The injection rate. Column (6) and (7): The minimum and maximum Lorentz factor of the injected electrons. Column (8): The spectral index of the injected electron spectrum. Column (9): The electron escape efficiency. Column (10): The acceleration timescale in units of the dynamical timescale. Column (11) and (12): The momentum diffusion coefficient and equipartition parameter derived from the SED modeling.

taken in 2009 January–June and 2013 January–March, respectively. The 4.5-month-long MWL campaign in 2009 collected an extensive multifrequency data set that is simultaneous and a good representation of the typical SED from Mrk 421 in a relatively low flux state. During the campaign in 2013, the source was in a historically low-activity state, and four SED snapshots were constructed. In particular, Mrk 421 exhibited exceptionally low X-ray and TeV flux on 2013 January 10 (MJD 56302) and 20 (MJD 56312).

In Fig. 5, we show the simultaneous X-ray and TeV γ -ray spectra on 2013 January 10 and those from the 2009 campaign, along with the theoretical SEDs reproduced by our model for comparison. The theoretical X-ray spectra are obtained using a quasi-equilibrium EED resulting from continual electron injection, and the resulting EEDs for two SEDs are shown in the right panel of Fig. 5. In our modeling, the three parameters ν_{pk} , $\gamma'_{i,\text{max}}$ and p are adjusted to reproduce the shape of the observed X-ray spectra, and the other four parameters δ_D , B' , R' and q'_0 are mainly determined on the basis of the X-ray and TeV γ -ray flux, as well as to avoid superluminal escape of electrons. Since we have not taken into account simultaneous radio and optical-UV data, which may be contaminated by contributions from larger-scale jet radiation, the values of η_{esc} and $\gamma'_{i,\text{min}}$ cannot be effectively constrained. In the current SED modeling, $\eta_{\text{esc}} = 1.26$ is chosen to yield a standard spectral index of ~ 2.2 , resulting from continuous injection of mono-energetic electrons with Lorentz factor well below the equilibrium Lorentz factor (e.g., Hu & Yan 2021). The continuously injected electrons with power-law spectra lead to a harder EED with a power-law index of ~ 2.0 in the low-energy part compared to the mono-energetic injection. Meanwhile, we set $\gamma'_{i,\text{min}}$ to 2×10^3 , which is roughly equivalent to the ratio of proton mass to electron mass, m_p/m_e .

The input model parameters and our interested physical quantities inferred from the observed SEDs are reported in Tab. 2. It can be seen that the global properties of the quasi-stationary zone and the diffusion coefficient D_0 (or t'_{acc}) inferred from the two SEDs do not differ substantially, although the value of ν_{pk} derived from the daily SED on MJD 56302 is a factor of five smaller in comparison with the typical SED accumulated over 4.5 months (also see Fig. 5). The inferred values of D_0 are similar to those obtained in previous works for Mrk 421 (Lewis et al. 2016; Hu et al. 2023), and for other HBLs (e.g., Hu & Yan 2021).

Moreover, our results show that the deduced Doppler factor, magnetic field and the blob size are comparable to previous estimations of Mrk 421 from SED modeling (Mankuzhiyil et al. 2011; Abdo et al. 2011; Baloković et al. 2016). We also note that the modeling of the daily SED on MJD 56302 yields the equipartition parameter U'_e/U'_B that is much closer to unity, and it differs substantially from that resulting from the typical SED in 2009. An attractive feature is that the equipartition can minimize the jet power (e.g., Finke et al. 2008). The difference in the physical quantity is driven mostly by the significantly larger electron energy density U'_e required by the SED modeling of Mrk 421 in 2009. This may be consistent with the fact that, besides quiescent episodes, the 2009 observations could contain a large number of similarly short flaring events that may be potentially linked to the electron injections. As can be seen from Fig. 2, the levels of observed X-ray fluxes in 6 out of the 10 selected epochs are very similar to those measured in the 2009 MWL campaign.

Additionally, we note that the observed X-ray fluxes in all 10 epochs are higher than those observed in the extremely low-activity state in 2013. Therefore, the theoretical SED that corresponds to the low-activity state may serve as an estimate for the background radiation of

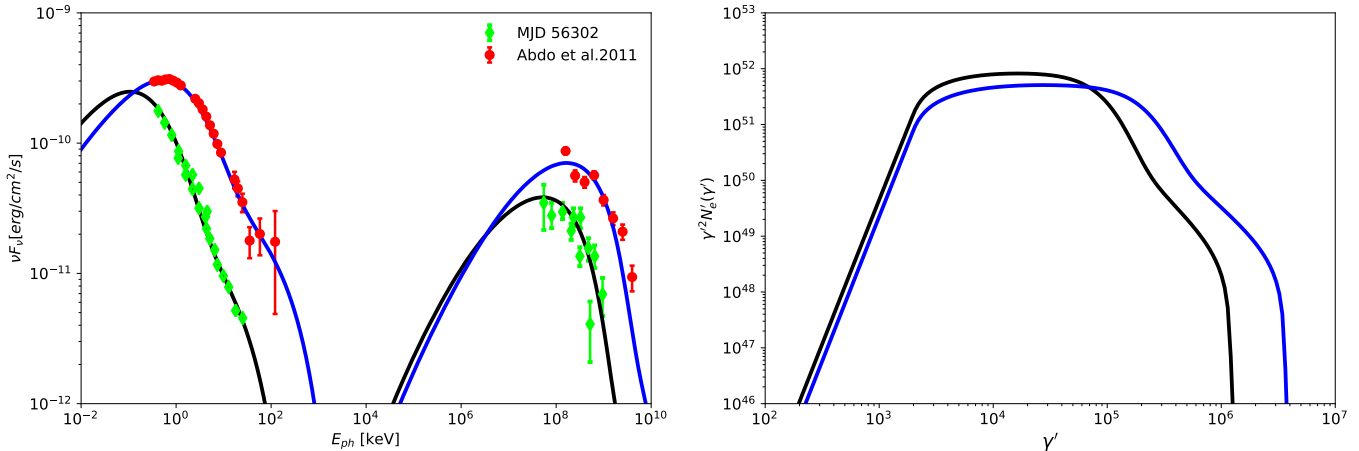


Figure 5. Modeling of the simultaneous X-ray and TeV γ -ray spectrum constructed in 2009 and 2013 MWL campaigns.

Mrk 421, and is used to decompose the X-ray spectrum observed in the 10 epochs.

4.3. Modeling X-ray spectrum and lag-frequency

In this section, we aim to simultaneously account for both the broadband X-ray spectrum and the time lags observed during 10 observations. For each observation, a comparison of the observed results and the simulated results is shown in Fig. 6. In the course of the fitting, $\gamma'_{i,\min} = 2 \times 10^3$ and $\eta_{\text{esc}} = 1.26$ are always held fixed, and the remaining seven parameters listed in Tab. 4 are allowed to vary.

Since the lack of simultaneous TeV γ -ray observations hinders our ability to effectively constrain the jet properties, we refer to the simultaneous X-ray and TeV γ -ray data from the flaring activity in March 2010 (Aleksić et al. 2015) as a benchmark for adjusting the parameters used to describe the X-ray spectrum in our study. To illustrate the spectral and flux range of variability, we present the daily SEDs on MJD 55265 and MJD 55277, which represent the highest and lowest flux levels during the flaring activity, respectively. The simultaneous data are shown in all plots of Fig. 6 as denoted by gray solid squares and empty circles, respectively.

In the modeling, we qualitatively fit the observed X-ray spectrum from 10 observations, using the steady-state solution generated by electrons that are continuously injected into the jet. The steady-state SSC model approach allows us to observe basic physical parameters averaged over the observation in the variable blob (e.g., Lewis et al. 2016, 2018; Diltz et al. 2015; Diltz & Böttcher 2016; Hu & Yan 2021).

As indicated by the fractional variability amplitude reported in Tab. 2, which increases with energy, one

may argue that the X-ray flux variability is not dominated by changes in the global properties (B' , R' and δ_D), but rather produced by variations in the emitting electron spectrum with the strongest variations occurring in the highest-energy electrons. Besides, the diffusion coefficient D_0 is not likely to vary on the same timescales as the observed X-ray emission (Lewis et al. 2016; Diltz et al. 2015). For simplicity, the theoretical LCs are produced with the assumption of an impulsive injection of electrons, and then the standard DFTs for the resulting LCs are performed to give the theoretical lag-frequency spectra (Appendix D). To intuitively understand the results, the time lags are measured using the CCF centroid, which is very reliable for a single smooth flare event. In order to be consistent with the basic assumption of spatial homogeneity, we require the injection time t'_{inj} to be longer than $t'_{\text{dyn}} = R'/c$ (e.g., Li & Kusunose 2000). Without loss of generality, we apply a constant injection with duration of $2R'/c$ to the injection rate of the electrons to produce the theoretical LCs in different bandpasses.

Both the observed CCF and Fourier time lags may provide important clues about the underlying physical processes. Since the former may represent mixed results for a pair of the complex and structured LCs, it would be inappropriate to attempt to model those results with the CCF centroid measured from a pair of simulated LCs generated by a single impulsive injection. However, the Fourier time lags caused by acceleration or cooling processes do not depend on the time envelope of the

Table 4. Input model parameters and derived quantities for the daily X-ray spectrum from 10 observations.

Obs. ID	δ_D	B'	R'	$\nu_{pk}(E_{pk})$	q'_0	$\gamma'_{i,max}$	p	t'_{acc}	D_0	U'_e/U'_B
		G	10^{15}cm	10^{17}Hz (keV)	s^{-1}	10^5		R'/c	10^{-6}s^{-1}	
(1)	(2)	(3)	(4)	(5)	(6)	(7)	(8)	(9)	(10)	(11)
0099280301	42	0.23	1.7	7.0(2.89)	1.06×10^{46}	0.9	2.30	1.82	2.42	8.0
0136540701	25	0.17	3.2	3.0(1.24)	2.18×10^{44}	13.0	1.78	1.80	1.30	13.9
0136541001	28	0.11	3.2	11.5(4.76)	2.54×10^{46}	2.0	2.35	1.86	1.26	18.8
0158970101	30	0.23	2.3	2.0(0.83)	6.30×10^{45}	5.0	2.25	2.13	1.53	4.6
0150498701	40	0.20	2.5	2.5(1.03)	1.46×10^{45}	7.0	2.10	2.50	1.20	5.7
0158971201	47	0.14	1.7	38.0(15.7)	8.44×10^{45}	3.0	2.25	1.74	2.53	33.4
0158971301	43	0.15	3.0	5.0(2.07)	2.63×10^{46}	2.0	2.40	2.35	1.06	8.2
0302180101	38	0.22	1.6	8.0(3.31)	3.55×10^{45}	10.0	2.20	1.84	2.54	9.4
0411080301	53	0.10	2.0	9.0(3.72)	1.92×10^{44}	5.5	1.95	5.36	0.70	51.4
0502030101	36	0.17	3.0	5.5(2.27)	2.62×10^{46}	2.0	2.35	1.70	1.47	7.3
$\langle \cdot \rangle$	38	0.17	2.4	9.2(3.8)	1.09×10^{46}	5.0	2.19	2.31	1.6	16.1

NOTE— Column (1) : Observation ID. Here, we fixed $\gamma'_{i,min} = 2 \times 10^3$ and $\eta_{esc} = 1.26$.

electron injection ⁷. We intend to mainly reproduce the lag-frequency spectra measured between the main hard (2–10 keV) and soft (0.5–2 keV) bands, which is the most frequently used in the spectral and temporal analysis of the X-ray variability. To impose a better constraint on the model parameters, we further reproduce the lag-frequency spectra measured between 2–10 keV and 1–2 keV. In Fig. 6, we also show the corresponding CCF lags measured from the simulated and observed LCs.

From Fig. 6, it can be seen that the theoretical X-ray spectrum agrees fairly well with the observational data, while our model satisfactorily describes the lag-frequency spectra combined with τ_1 and τ_2 . Moreover, we note that the CCF lags resulting from the simulated LCs are consistent with those resulting from the observed LCs, except for Obs. IDs: 0136541001, 0158971301 and 0411080301.

As can be seen from Tab. 4, the successful fits for the 10 epochs indicate that the inferred Doppler factor δ_D lies in a reasonable range of 25–53. According to [Hervet et al. \(2019\)](#), a perturbation with a high $\delta_D > 30$ crossing multiple recollimation shocks is required to interpret

the X-ray variability pattern of Mrk 421 observed by Swift-XRT during 13 years of observation. Such a high value of δ_D is also required in the study performed by [Banerjee et al. \(2019\)](#) on the time-dependent modeling of Mrk 421 in an internal shock scenario. Alternatively, the emitting plasma blobs with a high δ_D are easily produced in the plasmoid-driven reconnection framework (e.g., [Giannios et al. 2009](#); [Giannios 2013](#); [Petropoulou et al. 2016](#)). When the magnetization is high enough, the Lorentz factor of these plasma blobs in the rest frame of the jet can be as high as 50.

Meanwhile, we note that the size of the active zones R' lies in the range $(1.6–3.2) \times 10^{15}$ cm, which is smaller by a factor of about 6–12 compared to the quasi-stationary zone. Combined with the large δ_D , the significantly smaller R' gives rise to the rapid variability with characteristic time scale of the order of a few thousand seconds, which are consistent with the observations.

Moreover, the successful model parameters yield U'_e/U'_B that significantly depart from equipartition in the range $\sim 5–51$. This suggests that the high-energy emission from Mrk 421 may be produced in a kinetic energy flux-dominated jet. Such a departure from equipartition has often been reported in various studies for Mrk 421 during the different active states changing on the sub-hour-to-day timescales (e.g., [Shukla et al. 2012](#); [Aleksić et al. 2012, 2015](#); [Sinha et al. 2016](#)). Particularly, the departure was revealed by the SED modeling with an internal shock model ([Banerjee et al. 2019](#)). In the context of our model, this is mostly related to the increase in the electron injection rate ($\propto q'_0/R'^3$), which is more than two to three orders of magnitude larger than in the quasi-stationary zone. Meanwhile, the power-law index

⁷ It is worth noting that the LC observed in a single observation is only a random realization of the intrinsic variability that may be characterized by a PSD with a power-law form (i.e., colored noise) ([Timmer & Koenig 1995](#); [Emmanoulopoulos et al. 2013](#)). Thus, it may be more reasonable to simulate theoretical LCs numerically with the assumption of an injection with a random time envelope, resulting in a colored noise component. However, this does not affect the calculation of time lag in the frequency domain (see Appendix D.2). Moreover, this will introduce a variety of additional parameters that are not well known, and the simulated LC is typically not directly compared with the observed LC.

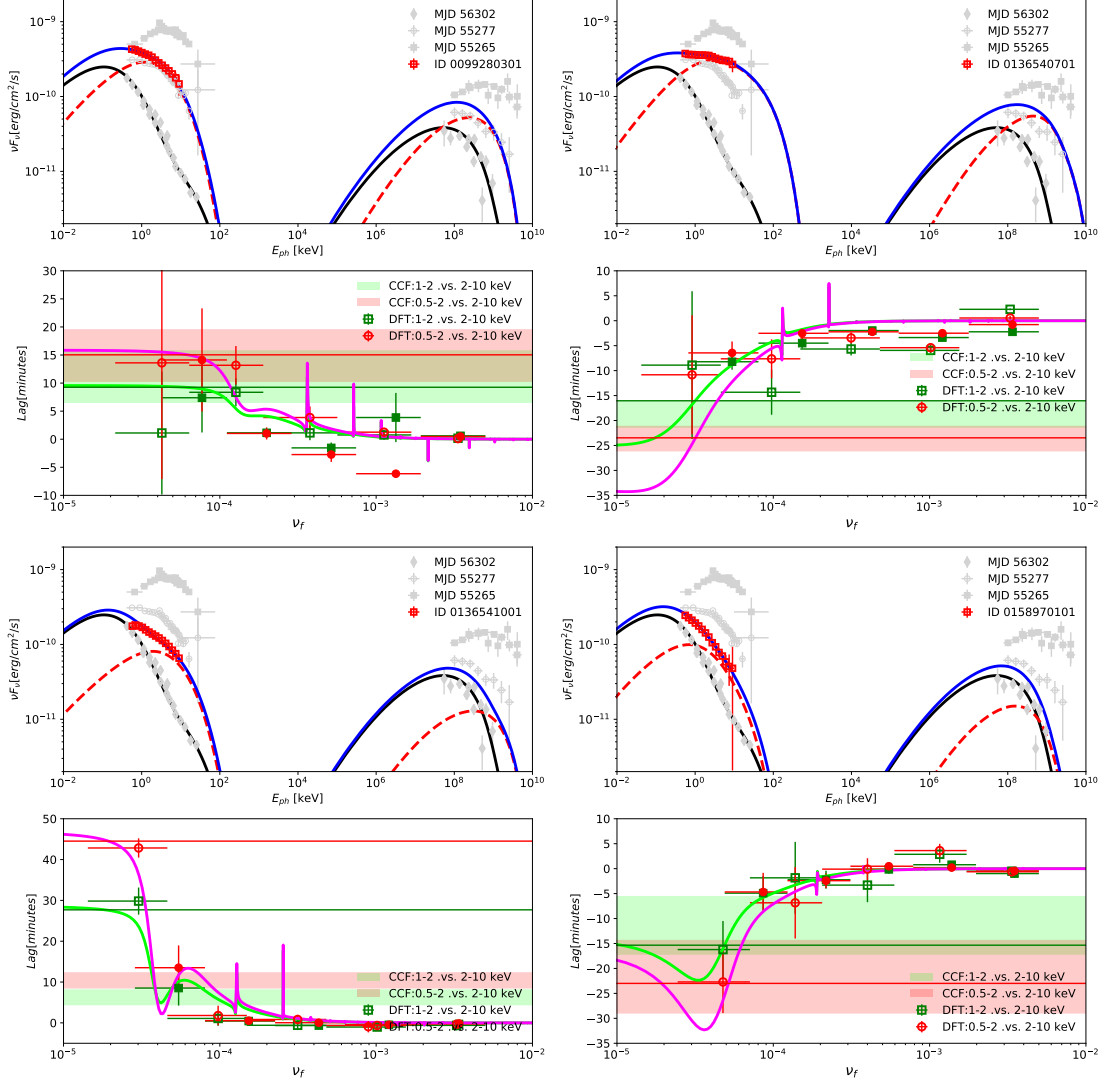


Figure 6. Modeling of the 0.5–10 keV X-ray spectrum and the Fourier time lags observed in different epoch. In the upper part of each panel, filled gray diamonds represent the simultaneous X-ray and TeV γ -ray data points on 2013 January 10, as reported in Baloković et al. (2016). The black squares and dark gray circles show the high- and low-state SEDs during flare activity in March 2010, respectively. The data points are taken from Aleksić et al. (2015). The red dashed lines and gray solid lines denote the SEDs from the non-stationary and quasi-stationary zone, respectively. The blue solid lines denote the total SED from two zones. In the lower part of each panel, the magenta and green solid lines respectively represent the theoretically predicted lag-frequency time lags for the 2–10 keV band with respect to the 0.5–2 and 1–2 keV bands, while the corresponding CCF time lags resulting from our model are denoted by the horizontal red and green lines, respectively.

of the injected electron spectrum is smaller than 2.5–2.7 inferred from the modeling of accurately measured X-ray spectra during the low-activity states in 2009 and 2013. This suggests that the energetic electrons injected into the active and quasi-stationary zones may be associated with different acceleration mechanisms (see discussion in Section 5.2).

Another significant difference is the diffusion coefficient. The modeling indicates that D_0 in the active

zones ranges from $(0.7 - 2.54) \times 10^{-6}$, which is about a factor of 3–10 larger than the quasi-stationary zone.

The differences in the physical properties of the two zones may support the idea that the active zones and the quasi-stationary zone correspond to physically distinct regions within the jet.

On the other hand, comparing the physical properties of the active zones responsible for the similar shape and flux level of X-ray emission reveals that the main differences may be related to changes in the diffusion

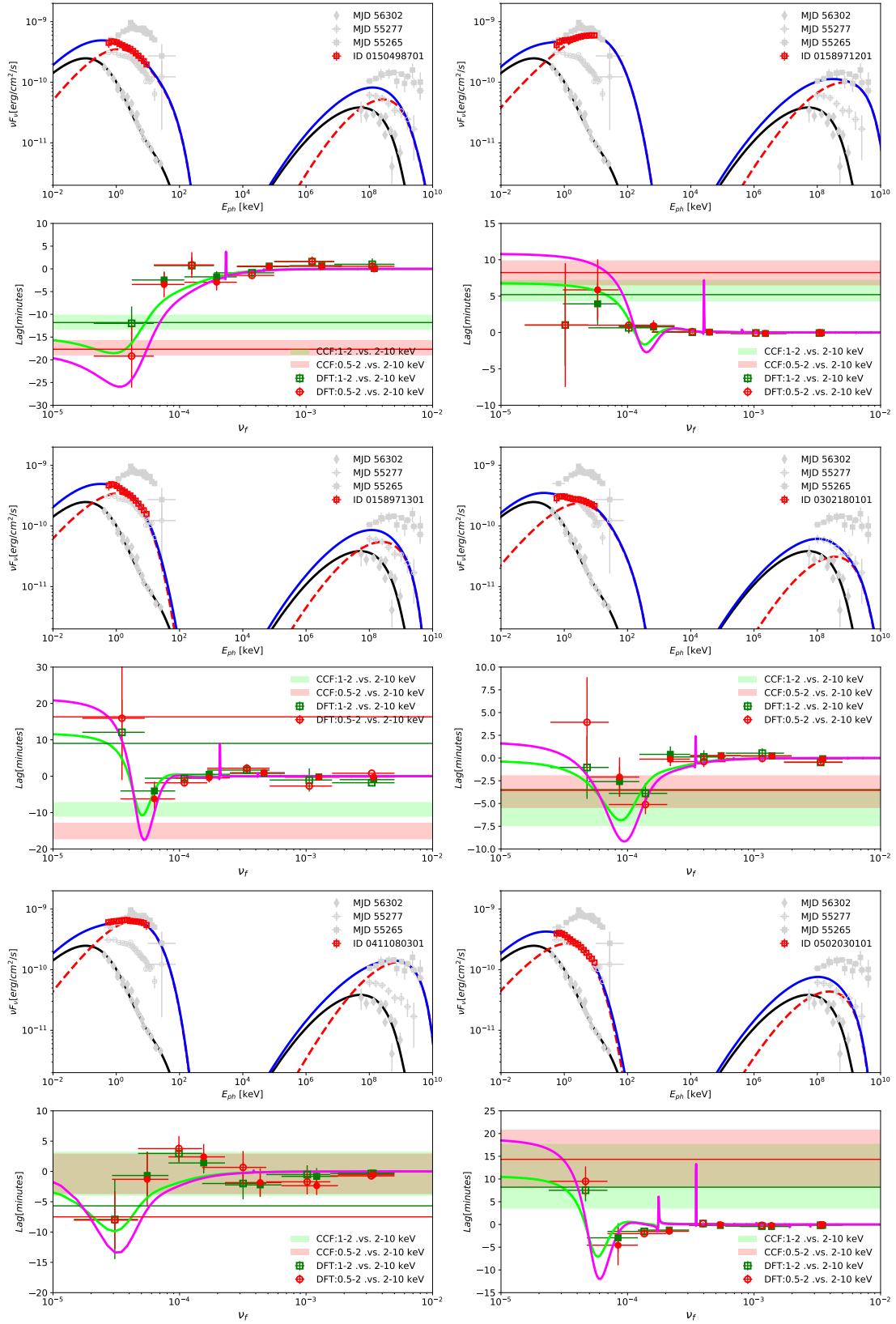


Figure 6. continued.

coefficient D_0 and/or the physical quantities related to the electron injection spectrum (i.e., $\gamma'_{i,\max}$ and p). These quantities are key in determining the presence of soft or hard time lags. The global properties of the blobs (B' , δ_D and R') vary within a factor of about two, which is associated with the observed time lags.

5. DISCUSSION

5.1. dependence of time lags on the model parameters

The time lags measured between LCs at different bands are an extraordinary opportunity to break degeneracies of the physical quantities involved in the SED modeling. Based on the analytic solutions to the electron transport equation in the Fourier domain, [Finke & Becker \(2014\)](#) explored the behaviors of Fourier time lags associated with variability in blazars. However, the authors do not take into account electron acceleration in the model, and therefore it was only able to produce soft time lags. To explain the formation of the hard time lags in blazar jets, [Lewis et al. \(2016\)](#) further extended the approach and developed an analytical physical model incorporating stochastic acceleration, shock acceleration, synchrotron cooling, adiabatic expansion, and electron escape regulated by Bohm diffusion. The model is able to qualitatively reproduce the hard time lags observed in the 1998 April 21 flare from Mrk 421, as obtained using *BeppoSAX*, as well as the X-ray spectrum observed at the peak of the flare. The authors indicated that the hard time lags and the peak X-ray spectrum require two populations of mono-energetic seed electrons, which have very different origins and undergo very different levels of shock acceleration and adiabatic losses.

In the context of our model, the observed X-ray spectrum is considered to be a sum of the flux of the quiescent background component and the active component, while the X-ray flux variation and the associated lags are mainly caused by the active component. In our model, the use of a power-law distribution for the electron injection spectra is motivated by two physically well-known dissipation processes: magnetic reconnection events and shocks. Compared with previous works, our model can simultaneously produce the observed X-ray spectrum and both the soft and hard time lags using the same set of parameters. It is necessary to show how the Fourier time lag profiles and the CCF lags vary, when the simultaneous X-ray and TeV γ -ray spectrum are kept relatively constant by changing multiple physical quantities over a physically appropriate range at once.

We perform the study by varying model parameters with respect to two baseline models, referred to as Cases A and B. In Case A, the electrons responsible for the hard X-ray emission are dominated by the radiative

cooling process, while in Case B, they are dominated by the acceleration process. Our baseline parameter values for Cases A and B are selected to reproduce the strictly simultaneous X-ray and TeV γ -ray data of Mrk 421 on MJD 55277, which represents the typical shape of the X-ray spectrum observed in Mrk 421. The detailed discussions are given in Appendix E, where the two baseline models are plotted in Fig. 11, with baseline parameters reported in Tab. 6. In Appendix E, we also show the effects of changing the parameters associated with the properties of the turbulence wave and the injected electron spectra. The results indicate that the X-ray time lags can greatly constrain the jet physics and offer valuable insights into the underlying mechanisms at work in the jet.

Given the theoretical prediction in Section 2, the magnetic field strength and Doppler factor are two critical parameters for determining the measured time lags. On the other hand, it is worth noting that the time lags may be related to the light-crossing timescale determined by the size of the active zone. Meanwhile, the global properties of the active zone are important to determine the cutoff of the TeV γ -ray spectrum. Here, we mainly illustrate the effects of variations in B' , δ_D and R' .

Fig. 7 is designed to depict the dependence of the resulting SED and time lags on the parameters involved. We decrease the strength of the magnetic field from $B' = 0.15$ G to $B' = 0.08$ G. To keep the Compton dominance approximately constant, we counterbalance the decrease in B' by increasing R' (Case A5 and B5) or δ_D (Case A6 and B6). The adjustments of q'_0 and $\gamma'_{i,\max}$ (or ν_{pk}) are required to ensure that the synchrotron spectrum remains relatively constant. From the view of the produced SEDs, the difference in the resultant TeV γ -ray spectrum is visible. Specifically, the SSC spectrum tends to shift toward higher energies as B' decreases, and further increases in δ_D results in a further shift of the component toward the high-energy end.

On the other hand, the measured $|\tau_c|$ increases with the decrease of B' (Case A5 and B5), and then decreases with the increase of δ_D (Case A6 and B6). The ratios of the CCF lags in Case A5 and A6 with respect to that in Case A are respectively $\tau_{c,A5}/\tau_{c,A} \simeq 2.7$ and $\tau_{c,A6}/\tau_{c,A} \simeq 2.0$, approximately equal to $\sqrt{B'_A{}^3/B'_A5{}^3} \simeq 2.6$ and $\sqrt{\delta_{D,A} B'_A{}^3/\delta_{D,A5} B'_A5{}^3} \simeq 2.2$. The ratios $\tau_{c,B5}/\tau_{c,B} \simeq 2.7$ and $\tau_{c,B6}/\tau_{c,B} \simeq 2.2$ are in accord with the theoretical predication $\sqrt{\nu_{\text{pk},B} B'_B{}^3/\nu_{\text{pk},B5} B'_B5{}^3} \simeq 2.5$ and $\sqrt{\nu_{\text{pk},B} \delta_{D,B} B'_B{}^3/\nu_{\text{pk},B5} \delta_{D,B5} B'_B5{}^3} \simeq 2.1$.

Meanwhile, the time lags measured in the Fourier domain also exhibit a similar variation. The maximum time lags in the frequency-dependent spectra approximately double the CCF lags in Case A5 and A6. In

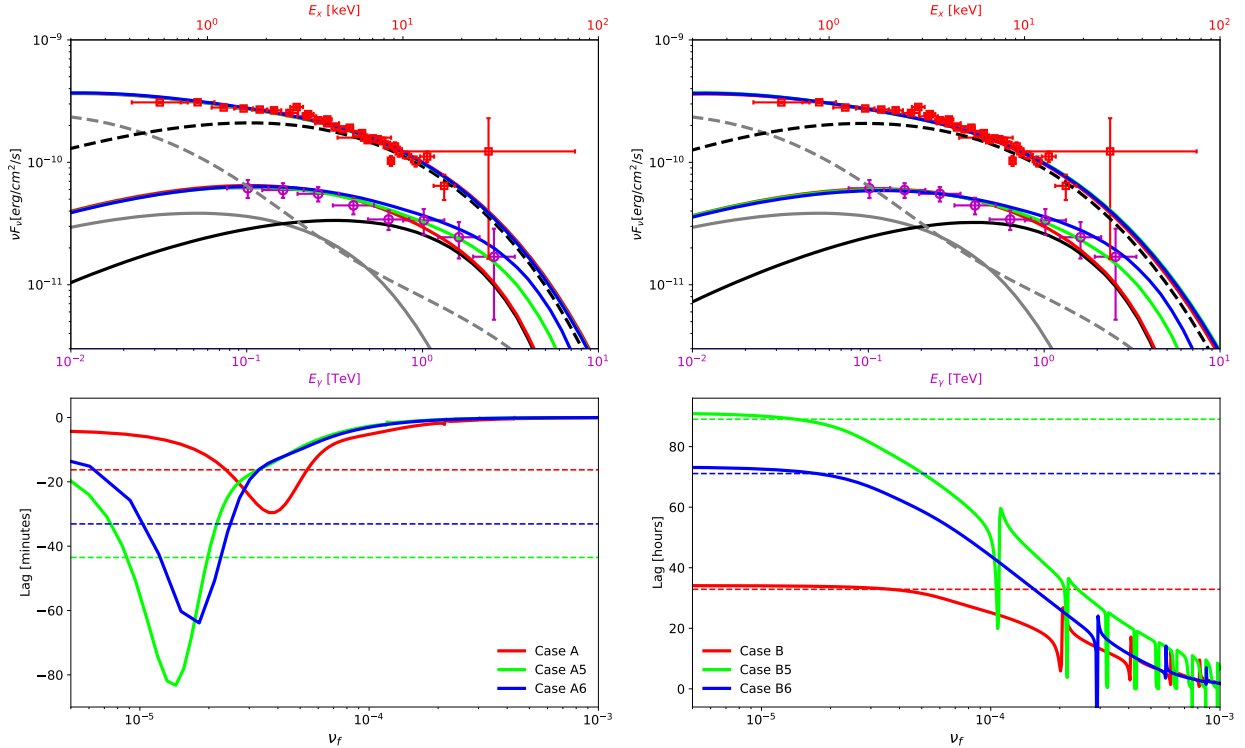


Figure 7. The theoretical SEDs (upper) and time lags (lower) resulting from variations in B' , δ_D and R' . In the lower panels, the Fourier time lag profiles for different cases are indicated in the legend, and the corresponding CCF lags are marked as horizontal lines. In the upper panels, the empty red squares and magenta circles represent the simultaneous X-ray and TeV γ -ray data on 2010 March 22 (MJD 55277), reported in [Aleksić et al. \(2015\)](#), respectively. The gray dashed and solid lines are the synchrotron and SSC spectrum from the (quasi-)stationary zone, respectively. The synchrotron and SSC spectrum from the non-stationary zone for Case A (left) and B (right) are denoted by the black dashed and solid lines, respectively. The red, green and blue solid lines are the SEDs from non-stationary zone that correspond to the three cases indicated by the legend of the lower panels, superimposed with the SED from the (quasi-)stationary zone.

Case B5 and B6, the CCF lags are comparable to the Fourier time lags at low frequencies.

The results demonstrate that the values of our interested physical quantities extracted using both X-ray spectra and the associated interband time lags may be in a well-constrained parameter space. Moreover, we conclude that the Fourier time lag spectra may be a more promising diagnostic of the nature of the underlying physical processes in blazar jets.

5.2. Variability and associated energy dissipation process

The rapidly variable emission may be related to impulsive magnetic reconnection events ([Giannios et al. 2009](#); [Giannios 2013](#)) or shocks ([Spada et al. 2001](#); [Böttcher & Baring 2019](#); [Chandra et al. 2021](#)) occurring in the relativistic jets. The two well-known energy dissipation processes can efficiently generate a population of electrons following the form of a power-law distribution. However, an important difference between these two mechanisms

is the magnetization of the dissipation region in the jets. When the jet is dominated by kinetic energy flux at the dissipation distance, the most natural candidate for powering the jet emission is shocks that transfer a significant fraction of the kinetic energy to electrons. On the other hand, in a magnetically dominated dissipation region, magnetic reconnection is a more likely mechanism for depositing magnetic energy into the radiating electrons.

Using all public XMM-Newton X-ray observations for Mrk 421, [Yan et al. \(2018\)](#) found that the distributions of the flare-profile parameters obey a power-law form that is a signature of a self-organized criticality model. Magnetic reconnection processes may therefore be supported. On the other hand, the detailed particle-in-cell (PIC) simulations show that the power-law index of the electron spectra formed in magnetic reconnection depends heavily on the plasma magnetization (e.g., [Cerutti et al. 2012](#); [Guo et al. 2014](#); [Sironi & Spitkovsky 2014](#); [Petropoulou et al. 2019](#)). For mild magnetization

$1 < \sigma < 10$, the electron spectra are characterized by a soft power-law index with $p \gtrsim 2$, whereas $p < 2$ for high magnetization $\sigma \gtrsim 10$. However, a direct result of this scenario is that the electron kinetic energy density and magnetic field energy density in the dissipation region are found in substantial equipartition, with an upper limit of $U'_e/U'_B \sim 3$ (Sironi et al. 2015). This is to be compared against our results that in all cases the inferred electron energy density substantially exceeds the magnetic energy density, by more than one order of magnitude. Thus, the magnetic reconnection process may be not expected to contribute significantly to the energetic electrons injected into the active blobs.

Shocks are a common phenomenon thought to occur in AGN jets. It is therefore natural to consider the possibility that the violent variability could be triggered by shock propagation inside the jet.

Brinkmann et al. (2005) compared the observed variability pattern with relativistic hydrodynamic simulations of a commonly accepted internal shock model for Mrk 421 emission. The authors indicated that LCs that looked similar to the observed ones could be represented by the numerically estimated flux superimposed with a substantial background emission of $\gtrsim 60\%$. Meanwhile, the results suggested that the observed emission of Mrk 421 may consist of at least two components: a quasi-stationary component and a flaring component.

Recently, Banerjee et al. (2019) carried out extensive simulations to study the SEDs of Mrk 421 during a giant outburst in February 2010. The authors showed that a time-dependent leptonic jet model in the internal shock scenario can successfully reproduce the SEDs in three spectral states, which represent the temporal evolution of Mrk 421 over a period of 5 days from a low- to high-flux state during the flaring event. Moreover, this scenario can produce significant spectral hardening from X-rays to TeV γ -rays, as well as the harder-when-brighter behavior in these energy bands. It is also interesting to note that the MWL spectral evolution during the giant outburst could be satisfactorily described by considering the emission from two connected regions, proposed by Dmytriiev et al. (2021). In the flare scenario, the steady-state emission arises from pre-accelerated electrons due to a stationary relativistic shock located in front of the emission region, referred to as the quiescent blob. The flaring emission is generated by transient turbulent regions where the pre-accelerated electrons escaping from the quiescent blob are injected and further accelerated via interaction with turbulent plasma waves excited by turbulent motion.

Alternatively, a realistic scenario could be a standing shock generated by the interaction of the upstream ex-

tended jet plasma with a turbulent ambient medium, or by recollimation in the jet. Such a scenario was proposed, based on the successful interpretation of the simultaneous MWL SED of Mrk 421 in the quiescent state (Abdo et al. 2011) and the flaring state (Aleksić et al. 2015). In particular, Hervet et al. (2019) probed the X-ray signature of recollimation shocks in the jet of Mrk 421. Using the *Swift*-XRT dataset spanning 13 years, they confirmed that the X-ray variability pattern of Mrk 421 is consistent with the scenario of the propagation of perturbations crossing the multiple stationary VLBI radio knots observed in the jet. It is in favor of the interpretation of slow/stationary radio knots as multiple recollimation shocks.

Indeed, the high X-ray polarization observed by Imaging X-ray Polarimetry Explorer provides important evidence for the shocks operating in the jet of Mrk 421 (Di Gesu et al. 2023). This is because the shock front partially aligns a previously disordered magnetic field.

The power-law form of electron distribution is a key feature of the shock mechanism. In the non-relativistic shock regime, both the linear theory and numerical simulations predict the power-law indices $p = (r+2)/(r-1)$ which are only determined by the compression ratio r (e.g., Drury 1983; Bell 1978; Ellison & Double 2004). The canonical index $p = 2$ is highlighted for strong shocks with $r = 4$. On the other hand, in the relativistic shock case, the power-law index depends critically on the nature and magnitude of turbulence, the shock speed, and the shock field obliquity. A nearly universal value of the index, $2.2 < p < 2.3$, is produced in the (semi-)analytic (Kirk & Heavens 1989; Kirk et al. 2000) and numerical studies of relativistic (quasi-)parallel shocks (e.g., Bednarz & Ostrowski 1998; Achterberg et al. 2001; Ellison & Double 2004; Niemiec & Ostrowski 2004; Crumley et al. 2019). A steeper spectrum with $p \simeq 2.5$ can be found under considering the modification of shock by the back-reaction of the accelerated particles (Kirk et al. 1996). Such a soft spectrum can also emerge from PIC kinetic plasma simulations where the Weibel instability enhances the turbulence (Sironi & Spitkovsky 2009; Sironi et al. 2013). Indeed, relativistic oblique shocks can result in a wide variety of power-law indices that vary dramatically with obliquity (Summerlin & Baring 2012; Baring et al. 2017). Generally, subluminal shocks possess indices in the range $1 < p < 2.5$, whereas superluminal shocks that possess higher obliquities have soft spectrum with $p > 2.5$.

Thus, the inferred spectral indices with $\langle p \rangle \simeq 2.2$ are compatible with the theoretical predictions of the shocks scenario. As expected from theoretical arguments, the energy dissipation at shocks does introduce a threshold

energy, below which the electrons are not freely able to cross the shock front and then no shock acceleration is in principle allowed (e.g., [Begelman & Kirk 1990](#)). For $p > 2$, the threshold energy is determined as

$$\gamma'_{\min} \simeq \Gamma_{\text{sh}} \frac{\epsilon_e m_p p - 2}{q m_e p - 1}, \quad (11)$$

where ϵ_e is the fraction of shock energy that goes into the electrons, Γ_{sh} is the bulk Lorentz factor of the shock in the upstream rest frame, and q is the number of pairs per proton ([Piran 1999](#); [Inoue & Tanaka 2016](#); [Böttcher & Dermer 2010](#)). For $q = 1$ and $\langle p \rangle = 2.2$, a relatively high energy, $\gamma'_{\min} \sim 0.17\epsilon_e \Gamma_{\text{sh}} m_p / m_e$, is required to cross the shock with the thickness that is expected to be of the order of the gyroradius of protons. Using $\Gamma_{\text{sh}} \sim \langle \Gamma \rangle = \langle \delta_D \rangle \sim 38$, gives $\gamma'_{\min} \sim m_p / m_e$ for a typical value of $\epsilon_e \sim 0.15$. According to the modeling of broadband SED from radio to TeV γ -rays, [Abdo et al. \(2011\)](#) proposed that the lower limit of γ'_{\min} can be from 2×10^2 up to 10^3 in order to reproduce the SMA and VLBA radio data. The higher value used should be reasonable for interpreting the X-ray spectrum and associated lags. In principle, the high minimum electron energy and the spectral index of injected electrons might be both reconciled with the relativistic proton-mediated shocks.

In conclusion, we suggest that shocks inside the jet may be more reasonable for powering the emission and triggering the rapid variability. Therefore, we could propose a picture that seed electrons are accelerated by randomly occurring shocks, which could provide a fully developed power-law spectrum (see discussion in [Tammi & Duffy 2009](#)). However, this process may be difficult to create any observable time lag signal because only a small amount of electrons in the upstream plasma, which is filled with a relatively low magnetic field, can pass through the shock, undergoing Fermi-I acceleration. Then, the accelerated electrons are injected downstream into the radiation zone, in which most of the observed radiation is being produced due to synchrotron and IC processes, while the energetic electrons may be further re-accelerated by turbulent plasma waves. Thus, a soft lag will be detected, when the stochastic acceleration in the radiation zone is less efficient than the acceleration in the vicinity of the shock, and the electron cooling processes dominate over the stochastic acceleration of electrons responsible for the emission at two compared bands. Conversely, a hard lag is expected to be observed.

6. SUMMARY

X-ray observations are a powerful diagnostic tool for understanding the physical processes taking place in the

jets. In the present paper, we reanalyzed 10 observations of the X-ray emission from HBL Mrk 421, each with an exposure of $\gtrsim 40$ ks, using the EPIC-pn instrument on board XMM-Newton. For each of the 10 observations, we obtained the averaged X-ray spectra in the 0.5 – 10 keV band and extracted 100s-binned LCs in six subbands: 0.5 – 1, 1 – 2, 2 – 4, 4 – 10 keV, as well as 0.5 – 2 and 2 – 10 keV bands. We derived the fractional rms variability amplitude F_{var} for the first four subbands and performed PSD analyses. The results of the analysis indicate that: (1) During the 10 observations, Mrk 421 exhibited significant variability in the X-ray band, and F_{var} increased with increasing energy. (2) The PSD of the variability follows a power law spectra above the white noise level up to $\sim 2 \times 10^{-4} - 2 \times 10^{-3}$ Hz, which corresponds to variability on timescales from minutes to an hour. Below the frequencies dominated by the white noise, the spectral index of the measured PSDs lies within the range of $\sim 1.9 - 3.0$, indicating that the variability amplitude rapidly decreases toward short timescales.

Particularly interesting information is the estimation of interband time lags associated with the variability in different subbands. These time lags can shed light on the acceleration as well as on the cooling mechanisms, and provide a powerful tool to constrain the physical properties of the jets. Then, the standard CCF and cross-spectral methods are employed to verify the existence and estimate the amount of the temporal lags between two LCs. Our results show that the CCF lags are comparable to the Fourier time lags at the lowest frequency bin. Moreover, we confirmed that the amount of the lags $|\tau|$ increases with the energy difference ΔE between the compared LCs. The trend in the plot of $\tau - \Delta E$ is in agreement with the linear relation expected by the synchrotron cooling or Fermi-type acceleration.

To extract the physical information of the jet contained in the X-ray spectra and the interband time lags measured by both the CCF and cross-spectral methods, we employed a self-consistent two-zone model, with a large emission region responsible for a quasi-stationary emission and a smaller region for highly variable emission. For each zone, we focused on the injection of electrons with a power-law energy distribution. We numerically solved a time-dependent transport equation that include synchrotron and Compton energy losses, hard-sphere stochastic acceleration, and escape. The model provides a very satisfactory description of the X-ray spectra and time delays for all of the observations. The physical quantities involved in the model can be well constrained by the CCF lag and the frequency-dependent lag spectra. We suggest that the main energy

dissipation process triggering rapid variability may be associated with shocks in the jets. However, magnetic reconnection should not be excluded in the scenario involving a weakly magnetized shock.

We thank the anonymous referee for constructive comments that helped improve and clarify the paper. This work is supported by the National Natural Science Foundation of China (NSFC-12263003, 12033006 and 12373016).

APPENDIX

A. LIGHT CURVES AND POWER SPECTRAL DENSITY

We show the X-ray LCs in the 1–2, 2–4, and 4–10 keV energy bands in the upper panels of all the plots in Fig. 8. To provide a visual method for comparing the variability amplitudes and possible time lags of the variability in the different energy bands, the LCs have been mean-subtracted and normalized by their standard deviation (de Marco et al. 2011). In most observations of Mrk 421, the LCs can be characterized by long-term trends lasting for timescales comparable to or longer than the duration of the observations, with short-term substructures superimposed on it. In Obs. ID 0502030101, LCs exhibit a long decaying phase, while LCs observed in Obs. ID 0158970101 display a decaying phase at the beginning followed by a rising phase.

The intrinsic variability power of the source can be represented by the power spectral density (PSD). For evaluating a PSD, the standard procedure is by calculating the periodogram, which is the modulus-squared of the Discrete Fourier Transform (DFT) of the observed X-ray LC. To give the same units as the PSD (i.e., $(rms/mean)^2$), the periodogram is further expressed as (e.g., Vaughan et al. 2003; Uttley et al. 2014)

$$I_j = \frac{2\Delta t}{\bar{x}^2 N} |\mathcal{X}_j|^2 \quad (\text{A1})$$

where \bar{x} is the mean flux of the LC, N the number of samples and Δt is the time bin⁸.

The normalized periodogram of the raw LC is an inconsistent estimator of the PSD, since its standard deviation at a frequency ν_f is 100%, leading to the large

scatter in the periodogram (e.g., Vaughan et al. 2003). The underlying PSD is obtained by fitting a given model to the normalized periodogram using the Markov Chain Monte Carlo (MCMC) method and maximum likelihood estimation (Vaughan 2010). For the fitting, we adopt a single power law (PL) model for the red noise continuum, plus a constant C to account for Poisson noise:

$$P(\nu_f) = A \left(\frac{\nu_f}{\nu_{\text{ref}}} \right)^{-\alpha} + C \quad (\text{A2})$$

where A is the normalization, α is the power-law slope index, and ν_{ref} is the reference frequency. In this approach, the fitting procedure for the considered model is equivalent to minimizing the following function

$$D = 2 \sum_{j=1}^{N/2} \left(\frac{I_j}{P_j} + \log P_j \right), \quad (\text{A3})$$

with I_j and P_j being the periodogram and the model PSD at frequency ν_j , respectively.

For this purpose, *emcee* sampler developed by Foreman-Mackey et al. (2013) is employed to obtain the posterior distribution of the model parameters. The median value of the posterior distribution is used as the best-fitting result of each parameter, while 16% and 84% quantiles give their uncertainties. The best-fitting results are shown in Fig. 8, and the power-law index α , logarithm of normalization $\log_{10} A$, and constant $\log_{10} C$ are tabulated in Tab. 5. Here, ν_{ref} is fixed to be the lowest frequency of the periodograms.

In the figure, we also present the frequency-binned periodograms obtained using the standard tool *pylag* for time series analysis (Uttley et al. 2014). In the calculations, the raw periodograms are binned into five logarithmically spaced bins, spanning from the lowest frequency T^{-1} (where T represents the total length of the LC used for variability analysis from each observation)

⁸ Note that integrating the normalized periodogram over a certain frequency range and taking the square root gives the fractional rms variability (i.e., F_{var}) contributed by variations over that frequency range.

up to the Nyquist frequency at 5×10^{-3} Hz. To obtain a more accurate PSD estimate, the LC is divided into two equal-length segments, and then a raw periodogram is calculated for each segment. Finally, the binned periodograms are obtained by binning the raw periodograms over frequency in a given frequency bin, as well as over both segments. From Fig. 8, it can be seen that the two rebinned PSDs are consistent with each other, and in agreement with the result of the Bayesian PSD analysis. This suggests that the binned periodograms offer reliable estimates of the underlying PSD, and the choice of bin size may be suitable. Thus, the binned method may be reasonable for variability analysis in this work.

B. CROSS-CORRELATION CENTROID DISTRIBUTIONS

Fig. 9 show the CCCDs from FR/RSS simulations for the selected 10 observations with durations of more than 40 ks.

C. FOURIER TRANSFORM AND TIME LAG

Below we provide a brief description of the DFT and the calculation of time lag in the Fourier frequency space.

Consider a light curve denoted as $x(t)$, consisting of N equidistant observations: $[t_j = j\Delta t, x(t_j)]$ for $j = 0, 1, \dots, N-1$, with a sampling interval Δt . The DFT of the data set is defined as follows:

$$\tilde{\mathcal{X}}(\omega_k) = \sum_{j=0}^{N-1} x(t_j) e^{-i\omega_k t_j} = \sum_{j=0}^{N-1} x(t_j) e^{-i2\pi k j / N}, \quad (\text{C4})$$

at each Fourier frequency $\omega_k = 2\pi\nu_k = 2\pi k / (N\Delta t)$ with $k = 0, 1, 2, \dots, N-1$. Here, ω_k represents the angular frequency in radians per second, and ν_k is in cycles per second (or Hertz). The minimum frequency is the inverse of the observation duration, i.e., $\nu_{\min} = 1/N\Delta t$. The maximum frequency is the Nyquist frequency $\nu_{\text{Ny}} = 1/2\Delta t$, based on the sampling theorem. For even N , we have $k_{\max} = N/2$, while for odd N , $k_{\max} = (N-1)/2$.

The Fourier time lag associated with variations in the soft-energy and hard-energy channels, ϵ_s and ϵ_h , is evaluated using the following relationship:

$$\tau(\omega_k) = \frac{\delta\phi(\omega_k)}{\omega_k} = \frac{\text{Arg} \left[\tilde{\mathcal{S}}(\omega_k) \tilde{\mathcal{H}}^*(\omega_k) \right]}{\omega_k}, \quad (\text{C5})$$

where $\delta\phi(\omega_k)$ denotes the phase lag for a given Fourier frequency ω_k , $\tilde{\mathcal{S}}(\omega_k)$ and $\tilde{\mathcal{H}}(\omega_k)$ represent the Fourier transforms of the two light curves $x_s(t_j)$ and $x_h(t_j)$, and the asterisk denotes the complex conjugate. In the given

context, a positive value signifies a hard lag, indicating that the hard channel signal lags behind the soft signal. Conversely, a negative value indicates a soft lag, with the soft channel signal lagging behind the hard signal.

D. NUMERICAL AND ANALYTICAL SOLUTION OF THEORETICAL TIME LAG

D.1. Numerical approach

Generally, the non-thermal, highly variable X-ray emission from blazars is attributed to the synchrotron emission of high-energy electrons in the jet. To directly compare with the observed LCs accumulated over certain energy intervals, the theoretical LCs integrated over corresponding range $[\epsilon_l, \epsilon_u]$ are calculated through

$$x(t) = \int_{\epsilon_l}^{\epsilon_u} F_{\epsilon}^{\text{syn}}(t) d\epsilon, \quad (\text{D6})$$

where $F_{\epsilon}^{\text{syn}}(t)$ is the synchrotron spectrum at the time t for a given energy $\epsilon m_e c^2$.

Since any variability on a time scale shorter than the light-crossing time of the system with a size R' should not be detectable in principle. To avoid causality violations, the light crossing effect should be considered in the calculations of the theoretical LCs. The observed synchrotron spectrum at the time t is calculated by (Zacharias & Schlickeiser 2013; Finke & Becker 2014)

$$F_{\epsilon}^{\text{syn}}(t) = \epsilon' F_0 \int_0^{t'_{lc}} dt' G(t'_{lc}, t') \times \int_1^{\infty} d\gamma' N'_e(\gamma', \frac{t\delta_D}{1+z} - t') R_{cs} \left(\frac{\epsilon'}{\epsilon'_c} \right), \quad (\text{D7})$$

where ϵ and ϵ' are related through $\epsilon' = \epsilon(1+z)/\delta_D$, $F_0 \equiv \frac{\sqrt{3}B'e^3\delta_D^4}{4\pi h d_L^2}$ with d_L denoting the luminosity distance of the source at the redshift z , $N'_e(\gamma', t')$ is the time-dependent solution of Eq. 8, and $G(t'_{lc}, t')$ is the geometrical weight function introduced by considering light travel time effects, given by

$$G(t'_{lc}, t') = \frac{6}{t'_{lc}} \left[\frac{t'}{t'_{lc}} - \left(\frac{t'}{t'_{lc}} \right)^2 \right], \quad (\text{D8})$$

where $t'_{lc} \equiv 2R'/c$ denotes the light-travel time across the entire blob.

Here, the function $R_{cs}(\epsilon'/\epsilon'_c)$ represents the monochromatic emission power averaged over a population of electrons with randomly distributed pitch angles (Crusius & Schlickeiser 1986), and $\epsilon'_c = \frac{3}{2} \frac{B'}{B_{cr}} \gamma'^2$ is the dimensionless characteristic synchrotron energy of electrons with the Lorentz factor γ' . To minimize computational costs, an efficient approximation provided by Finke et al. (2008) is adopted to calculate the function.

Table 5. The best-fitting parameters of a PL plus Poisson noise model fitted to the normalized periodograms of Mrk 421 in three energy bands: 1–2, 2–4 and 4–10 keV.

Obs ID	1–2 keV				2–4 keV				4–10 keV			
	$\log_{10}(A)$	$\log_{10} C$	α	t_v	$\log_{10}(A)$	$\log_{10} C$	α	t_v	$\log_{10}(A)$	$\log_{10} C$	α	t_v
(1)	(2)	(3)	(4)	(5)	(6)	(7)	(8)	(9)	(10)	(11)	(12)	(13)
0099280301	$2.38^{+0.60}_{-0.47}$	$-0.74^{+0.04}_{-0.05}$	$2.78^{+0.75}_{-0.57}$	58.7	$2.91^{+0.60}_{-0.47}$	$-0.19^{+0.04}_{-0.04}$	$2.89^{+0.72}_{-0.56}$	65.8	$3.18^{+0.50}_{-0.40}$	$0.19^{+0.04}_{-0.04}$	$2.61^{+0.57}_{-0.45}$	55.7
0136540701	$3.17^{+0.31}_{-0.27}$	$0.49^{+0.04}_{-0.04}$	$2.28^{+0.50}_{-0.22}$	77.8	$3.60^{+0.27}_{-0.21}$	$0.54^{+0.04}_{-0.04}$	$2.16^{+0.27}_{-0.12}$	44.6	$3.89^{+0.37}_{-0.32}$	$0.16^{+0.04}_{-0.04}$	$2.33^{+0.30}_{-0.25}$	29.2
0136541001	$2.87^{+0.48}_{-0.42}$	$-1.30^{+0.04}_{-0.04}$	$2.91^{+0.43}_{-0.39}$	43.0	$3.07^{+0.49}_{-0.44}$	$-0.80^{+0.04}_{-0.04}$	$2.83^{+0.48}_{-0.42}$	50.0	$2.93^{+0.47}_{-0.40}$	$-0.27^{+0.04}_{-0.04}$	$2.34^{+0.44}_{-0.36}$	50.0
0158970101	$2.04^{+0.33}_{-0.32}$	$-0.65^{+0.05}_{-0.05}$	$2.36^{+0.40}_{-0.42}$	49.4	$2.26^{+0.32}_{-0.32}$	$0.02^{+0.05}_{-0.04}$	$2.48^{+0.36}_{-0.44}$	85.2	$2.26^{+0.39}_{-0.34}$	$0.71^{+0.05}_{-0.05}$	$2.23^{+0.54}_{-0.70}$	137.6
0150498701	$2.72^{+0.35}_{-0.30}$	$-1.46^{+0.06}_{-0.06}$	$2.49^{+0.28}_{-0.24}$	16.6	$3.28^{+0.47}_{-0.38}$	$-0.98^{+0.05}_{-0.04}$	$3.04^{+0.43}_{-0.35}$	31.6	$3.49^{+0.48}_{-0.39}$	$-0.46^{+0.04}_{-0.04}$	$3.06^{+0.47}_{-0.38}$	40.7
0158971201	$3.29^{+0.29}_{-0.26}$	$-1.32^{+0.07}_{-0.08}$	$2.19^{+0.18}_{-0.17}$	8.5	$3.60^{+0.30}_{-0.27}$	$-0.92^{+0.08}_{-0.09}$	$2.15^{+0.19}_{-0.17}$	8.5	$3.90^{+0.32}_{-0.27}$	$-0.56^{+0.07}_{-0.08}$	$2.16^{+0.20}_{-0.18}$	9.3
0158971301	$2.97^{+0.45}_{-0.39}$	$-1.54^{+0.04}_{-0.04}$	$3.16^{+0.43}_{-0.36}$	36.6	$3.43^{+0.55}_{-0.45}$	$-0.99^{+0.04}_{-0.04}$	$3.42^{+0.55}_{-0.46}$	49.9	$3.60^{+0.55}_{-0.45}$	$-0.50^{+0.04}_{-0.04}$	$3.22^{+0.58}_{-0.47}$	52.1
0302180101	$1.84^{+0.38}_{-0.32}$	$-1.71^{+0.06}_{-0.07}$	$2.35^{+0.37}_{-0.31}$	20.9	$2.25^{+0.38}_{-0.32}$	$-1.19^{+0.06}_{-0.06}$	$2.33^{+0.36}_{-0.29}$	22.6	$2.89^{+0.48}_{-0.39}$	$-0.73^{+0.05}_{-0.06}$	$2.61^{+0.48}_{-0.39}$	27.8
0411080301	$2.70^{+0.52}_{-0.42}$	$-1.08^{+0.04}_{-0.04}$	$3.06^{+0.57}_{-0.46}$	66.3	$2.92^{+0.54}_{-0.43}$	$-0.64^{+0.03}_{-0.03}$	$2.91^{+0.55}_{-0.46}$	68.2	$3.24^{+0.54}_{-0.44}$	$-0.30^{+0.04}_{-0.03}$	$2.88^{+0.57}_{-0.46}$	67.2
0502030101	$2.30^{+0.32}_{-0.26}$	$-1.60^{+0.14}_{-0.19}$	$1.91^{+0.24}_{-0.18}$	6.4	$2.57^{+0.35}_{-0.30}$	$-1.12^{+0.09}_{-0.12}$	$1.98^{+0.26}_{-0.23}$	9.6	$2.70^{+0.40}_{-0.34}$	$-0.49^{+0.07}_{-0.09}$	$1.94^{+0.23}_{-0.28}$	15.9

NOTE— t_v is the shortest variability time scale (in units of minutes) derived from the PSD analysis.

Then, the X-ray time lag associated with the simulated LCs in the soft- and hard-energy channels is evaluated using the standard CCF and cross-spectral methods.

Since the additional Fourier time lag introduced by the light-crossing time effect is independent of the observing energy (see Appendix D.2). The frequency-dependent lag can be calculated by using the standard DFT method to the simulated LCs given by

$$F_{\epsilon}^{\text{syn}}(t) = \epsilon' F_0 \int_1^{\infty} d\gamma' N_e'(\gamma', \frac{t\delta_D}{1+z}) R_{\text{cs}} \left(\frac{\epsilon'}{\epsilon_c} \right), \quad (\text{D9})$$

where the light crossing effect is not taken into account for simplicity.

D.2. Analytical approach

Considering that the electron cooling is dominated by synchrotron radiation, and the acceleration, cooling and escape of the electrons are independent of t' , taking the Fourier transform of both sides of the transport equation (8) yields

$$\begin{aligned} \frac{i\omega'}{D_0} \tilde{\mathcal{N}}_e'(\gamma', \omega') &= \frac{\partial}{\partial \gamma'} \left\{ \gamma'^4 \frac{\partial}{\partial \gamma'} \left[\frac{\tilde{\mathcal{N}}_e'(\gamma', \omega')}{\gamma'^2} \right] \right\} \\ &- \frac{\partial}{\partial \gamma'} \left[(a\gamma' - b\gamma'^2) \tilde{\mathcal{N}}_e'(\gamma', \omega') \right] \\ &- \frac{\tilde{\mathcal{N}}_e'(\gamma', \omega')}{t'_{\text{esc}} D_0} + \frac{\tilde{f}'_e(\omega') q'_e(\gamma')}{D_0} \end{aligned} \quad (\text{D10})$$

where $a \equiv A_0^{\text{sh}}/D_0$, $b \equiv B_0/D_0$ and $B_0 \equiv \sigma_T B'^2/(6\pi m_e c)$ with the strength of the magnetic field B' , electron rest mass m_e , light speed c and Thomson

cross-section σ_T , and $\tilde{f}'_e(\omega')$ is the Fourier transform of the time-dependent injection profile $f'_e(t')$.

Following the standard method in Schlickeiser (1984), one can obtain the exact solution for the Fourier transform of the electron distribution

$$\begin{aligned} \tilde{\mathcal{N}}_G'(\omega', \gamma') &= \frac{q'_0 f'_e(\omega')}{b D_0 \gamma_0'^2} \left(\frac{\gamma'}{\gamma_0'} \right)^{a/2} e^{-b(\gamma' - \gamma_0')/2} \\ &\frac{\Gamma(\mu - \kappa + 1/2)}{\Gamma(1 + 2\mu)} M_{\kappa, \mu}(x_{\min}) W_{\kappa, \mu}(x_{\max}), \end{aligned} \quad (\text{D11})$$

for a mono-energetic electrons with Lorentz factor γ_0' , i.e., $Q'_e(\gamma', t') = f'_e(t') q'_0 \delta(\gamma' - \gamma_0')$. Here, the subscript ‘G’ is used to remind readers that it actually represents the Green function of Eq. D11, $\Gamma(\cdot)$ denotes the Gamma function, $M_{\kappa, \mu}(\cdot)$ and $W_{\kappa, \mu}(\cdot)$ are the Whittaker’s functions with the arguments x_{\min} and x_{\max} respectively given by

$$x_{\min} = \min(b\gamma', b\gamma_0'), \quad x_{\max} = \max(b\gamma', b\gamma_0'), \quad (\text{D12})$$

and the subscript indices κ and μ respectively defined as

$$\kappa = 2 + \frac{a}{2}, \quad \mu = \sqrt{\left(\frac{a+3}{2} \right)^2 + \frac{1}{D_0 t'_{\text{esc}}} + i \frac{\omega'}{D_0}}. \quad (\text{D13})$$

On the other hand, the exact steady-state solution resulting from monogenetic continuous injection can be straightforwardly obtained by simply removing the frequency-dependent factor in Eq. D11, and is given by

$$\begin{aligned} N'_e(\gamma') &= \frac{q'_0}{b D_0 \gamma_0'^2} \left(\frac{\gamma'}{\gamma_0'} \right)^{a/2} e^{-b(\gamma' - \gamma_0')/2} \\ &\times \frac{\Gamma(\mu - \kappa + 1/2)}{\Gamma(1 + 2\mu)} M_{\kappa, \mu}(x_{\min}) W_{\kappa, \mu}(x_{\max}), \end{aligned} \quad (\text{D14})$$

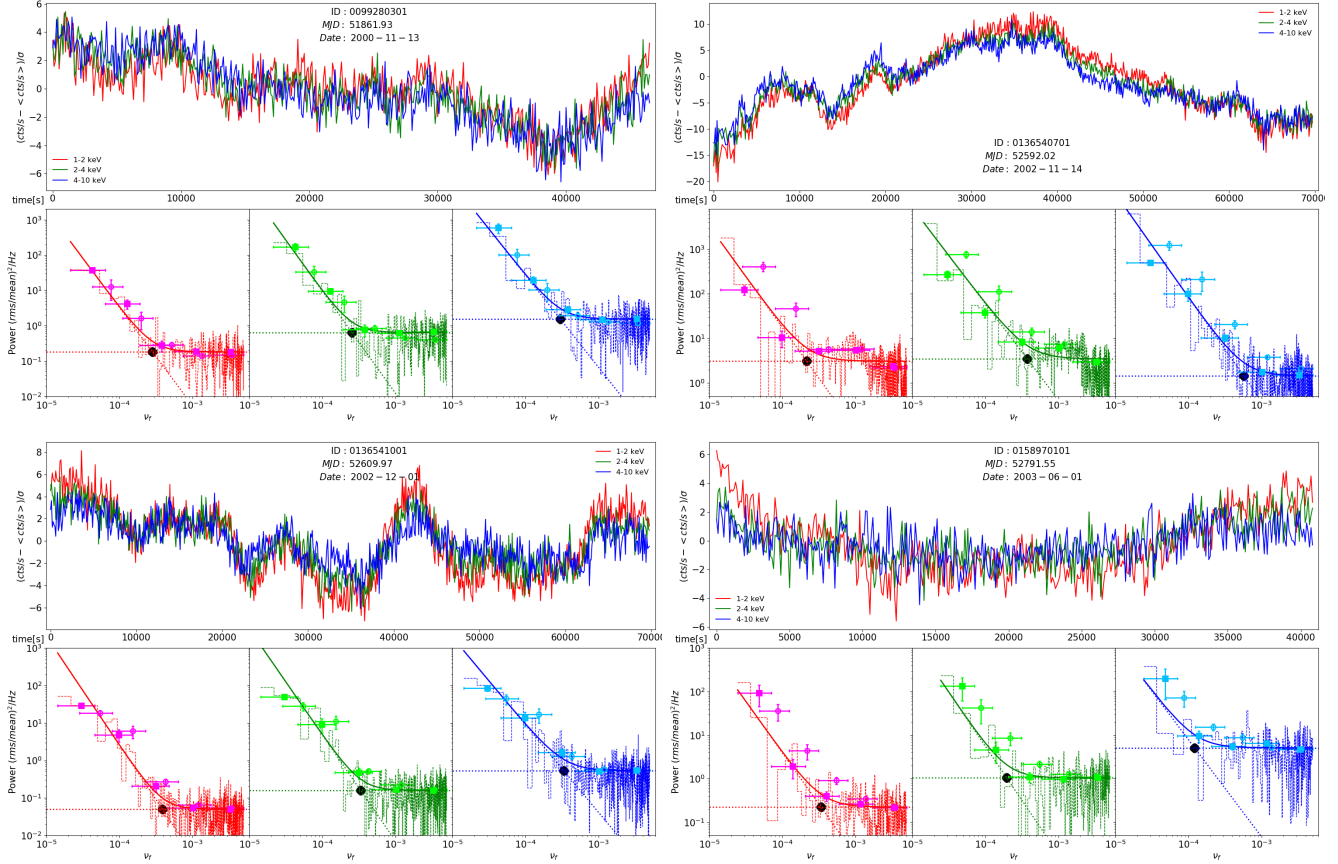


Figure 8. XMM-Newton EPIC-pn LCs and estimated power spectra of Mrk 421 obtained from 10 observations. In each panel, the upper part displays the LCs, while the lower part shows the corresponding PSDs. The RMS-squared normalization is applied such that the periodogram will be calculated in units consistent with the PSD. The solid lines represent the PSDs estimated using the Bayesian method, whereas the solid squares and empty circles correspond to two logarithmically rebinned versions of the PSDs. The black filled circle marks the frequency threshold above which the variability is dominated by Poisson noise. The dotted horizontal line marks the Poisson noise level for each band.

and

$$\kappa = 2 + \frac{a}{2}, \quad \mu = \sqrt{\left(\frac{a+3}{2}\right)^2 + \frac{1}{D_0 t'_{\text{esc}}}}. \quad (\text{D15})$$

Given the Fourier transformed electron distribution, the Fourier time lag associated with variations in two energy channels is calculated via Eq.C5 and the Fourier transform of synchrotron spectrum given by

$$\begin{aligned} \tilde{\mathcal{F}}_e^{\text{syn}}(\omega) &= \epsilon' F_0 \tilde{\mathcal{G}}(t'_{\text{lc}}, \omega') \frac{1+z}{\delta_{\text{D}}} \\ &\times \int_1^\infty d\gamma' \tilde{\mathcal{N}}'(\gamma', \omega') R_{\text{cs}} \left(\frac{\epsilon'}{\epsilon'_c} \right). \end{aligned} \quad (\text{D16})$$

where $\omega' = \omega(1+z)/\delta_{\text{D}}$, and the geometrical weight function in the Fourier domain $\tilde{\mathcal{G}}(t'_{\text{lc}}, \omega')$ is given by

$$\begin{aligned} \tilde{\mathcal{G}}(t'_{\text{lc}}, \omega') &= \int_0^{t'_{\text{lc}}} dt' e^{-i\omega' t'} G(t'_{\text{lc}}, t') \\ &= 6 \cdot \frac{e^{-i\omega' t'_{\text{lc}}} (i\omega' t'_{\text{lc}} + 2) + i\omega' t'_{\text{lc}} - 2}{i\omega' t'_{\text{lc}} \cdot (i\omega' t'_{\text{lc}})^2}. \end{aligned} \quad (\text{D17})$$

The function $\tilde{\mathcal{G}}(t'_{\text{lc}}, i\omega')$, representing the light-travel time effect, is independent of photon energy. Therefore, no observed time lag is related to the light-crossing time.

As indicated by the fact that the PSD of blazars resembles colored noise, it is more reasonable to assume that electrons are injected as a power law in the frequency domain. However, it can be seen from the time-dependent solution Eq.D11 that the phase lags measured from the argument of the cross-spectrum between two energy channels are independent of the precise form of $f'_e(\omega')$. Therefore, the form of $f'_e(\omega')$ or $f'_e(t')$ does not modify the lag-frequency spectra, although it is important to determine the PSD of variability.

For simplicity, we assume an instantaneous electron injection represented by the δ -function: $f_e(t') = \delta(t' - t'_0)$, in the present analysis. Taking the Fourier transform of $f_e(t')$ gives $f'_e(\omega') = e^{-i\omega' t'_0}$.

To demonstrate the validity of the numerical approach, comparisons are made with both analytical and

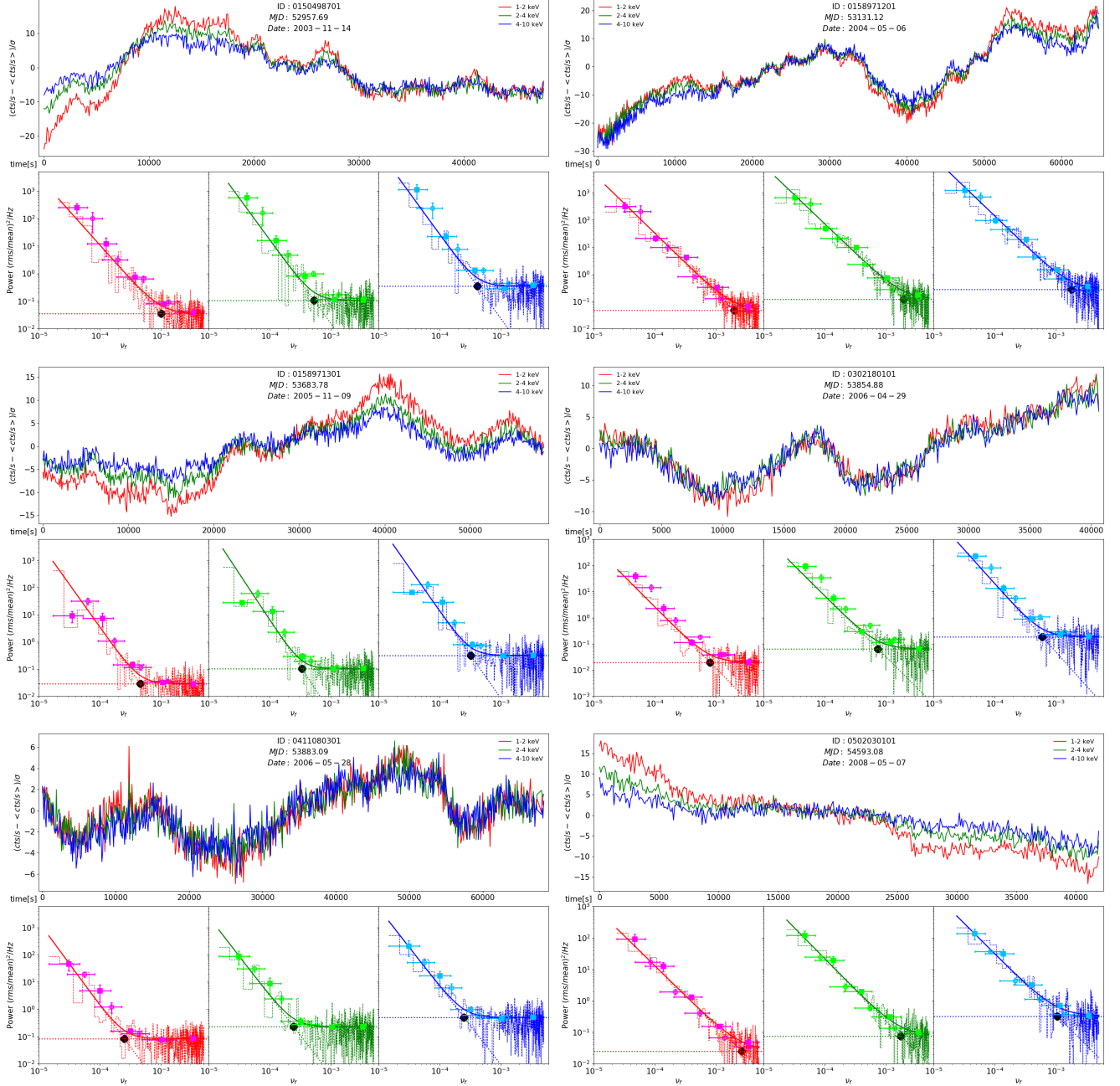


Figure 8. Continued.

numerical results. In the lower left panel of Fig.10, we show a comparison of the exact solution for the steady-state EED given by Eq.D14 with that computed using a bi-directional Runge-Kutta method. The resulting synchrotron and SSC spectrum are shown in the upper left panel of the figure. It can be seen that the numerical and analytical solutions are in good agreement. The model parameters are selected to produce the typical SED of Mrk 421 during the flaring state and are summarized as follows: $B' = 7.8 \times 10^{-2}$ G, $\delta_D = 45$, $R' = 3.3 \times 10^{15}$

cm, $\nu_{pk} = 10^{18}$ Hz, $\eta_{esc} = 0.67$, $D_0 = 5.51 \times 10^{-7} s^{-1}$, $q'_0 = 3.97 \times 10^{41} s^{-1}$ and $\gamma'_0 = 10^3$. With the given values of R' and δ_D , the derived dynamical timescale in the observer's frame t_{dyn} is about 0.7 hr.

With the parameters set for the steady-state SED, we can calculate the frequency-dependent X-ray time lags using the exact solution for the Fourier transformed EED given by Eq.D11. For illustrative purposes, we obtain the time delays of the 3, 5, and 7 keV energy channels relative to the 1.5 keV reference energy channel.

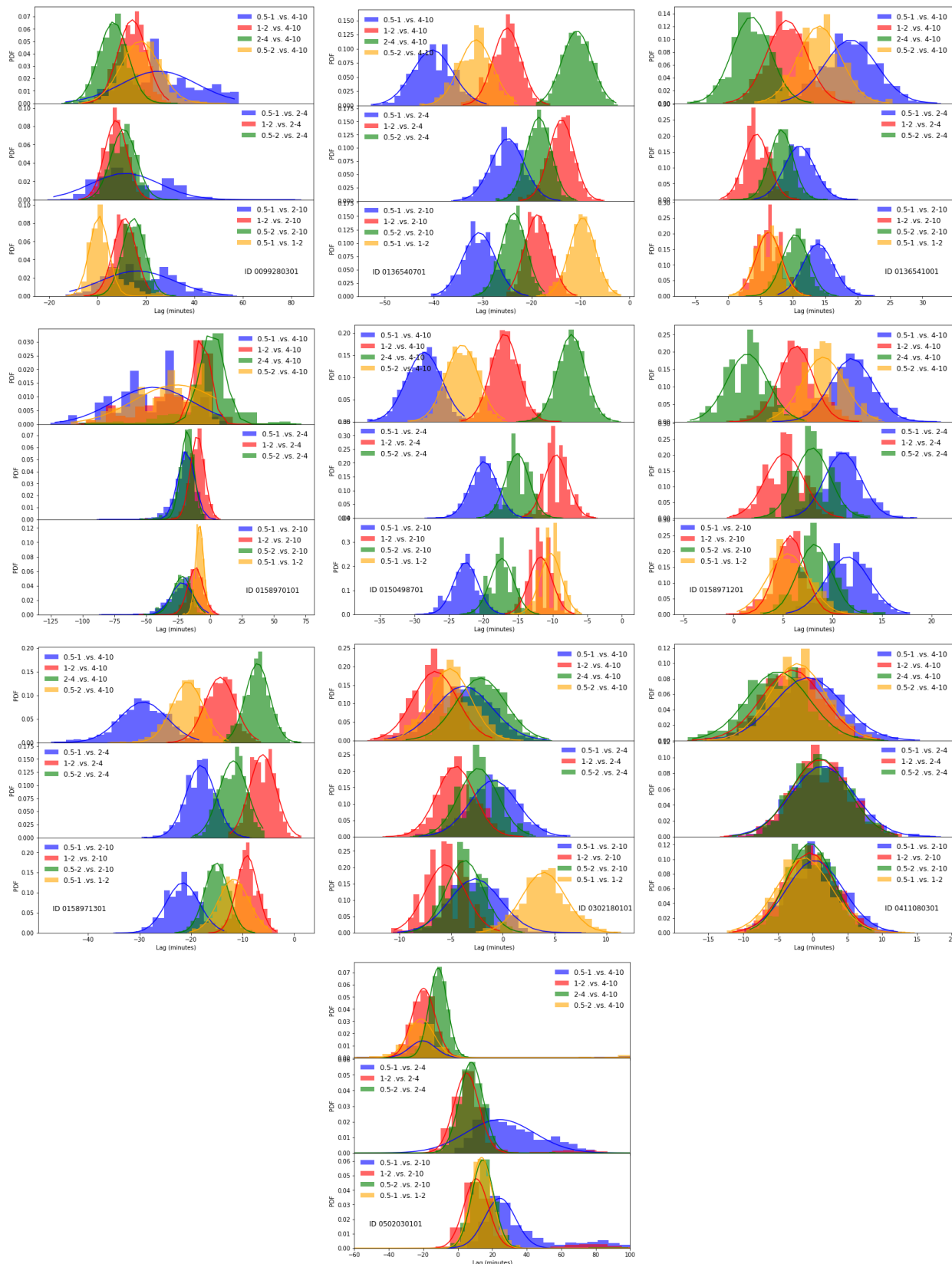


Figure 9. Cross-correlation centroid distributions from FR/RSS simulations. A Gaussian fit was used to derive the lag and its error.

The results are shown in the lower right panel of Fig.10, denoted by the gray solid, dashed, and dash-dotted lines, respectively.

To compare with the exact results, the X-ray LCs at the four mono-energy channels are calculated using the synchrotron spectrum given by Eq.(D7) and the time-dependent EED computed numerically by solving Eq.(8) for an instantaneous injection of mono-energetic electrons. Then, the frequency-dependent lags are directly calculated by applying the standard DFT to the resulting LCs (see Appendix C). The frequency-dependent lags between each energy channel and the 1.5 keV reference energy channel are displayed in the lower right of Fig.10, denoted by the thick blue, red, and green dotted lines, respectively. Our results indicate that the numerical and analytical Fourier time lag profiles appear in good agreement with each other below the frequency $\sim (0.75t_{lc})^{-1} \simeq 3 \times 10^{-4}$ Hz. It should be noted that Fourier frequencies higher than t_{lc}^{-1} are unphysical in the usual homogeneous model assumed here.

Moreover, we produce the integrated LCs in the five bandpasses: 1–2, 2–4, 4–6, 6–8, and 4–10 keV. The central energies of the first three bandpasses are 1.5, 3, and 5 keV, respectively, while both of the central energies of the last two bandpasses are 7 keV. The simulated LCs at various energy channels are shown in the upper right panel of Fig.10. Similarly, we calculate the time delays of each band with respect to the 1–2 keV reference band, represented by the thick blue, red, green, and black solid, respectively. We can see that the difference between the time delays resulting from the integrated LC pairs and mono-energy LC pairs increases with the energy difference between the two compared energy channels. Although the central energies of both 6–8 and 4–10 keV bandpasses are 7 keV, the time delays of 6–8 and 4–10 keV with respect to 1–2 keV differ significantly from the time delay calculated from the mono-energy LC pair: 1.5 and 7 keV. Thus, the simple estimation for the time lags between two mono-energy channels is not enough to represent the results between two observed LCs.

Using the integrated LCs in various bandpasses, the time lags measured by the CCF centroid are also shown in the lower right panel of Fig.10, denoted by the thin blue, red, green, and black dotted lines, respectively. The CCF lags between 1–2 and 2–4 keV bands are about 0.8 hr. The results indicate that the CCF lags appear in close agreement with the Fourier time lags at the low frequencies, where the Fourier lag spectrum weakly depends on the frequency.

E. EFFECTS OF CHANGING IN THE MODEL PARAMETERS

In this section, we present a detailed discussion about the effects of varying model parameters describing the properties of the turbulence wave and the injected electron spectra, with respect to two baseline models (Case A and B). Here, the time lag between two narrow bands: 1–2 and 4–10 keV is used for clarification.

Case A and B are plotted as the red and green solid lines in Fig. 11. Although it is difficult to distinguish between the two cases based on the produced SED, both the CCF lags and Fourier time-lag profiles are significantly different in the two cases. The differences are mainly attributed to the selected values of ν_{pk} (or D_0) and $\gamma'_{i,max}$, which are critical in determining whether the lag is detected as either a negative (soft) or a positive (hard) lag. A hard lag is observed when $\gamma'_{i,max}$ is well below the equilibrium Lorentz factor γ'_{eq} that is related to ν_{pk} through the relation $h\nu_{pk}/m_e c^2 = 1.5\epsilon_B \gamma_{eq}'^2 \delta_D / (1+z)$. Otherwise, a soft lag is detected. In the calculations, the values of γ'_{eq} are 1.6×10^5 and 2.2×10^5 for $h\nu_{pk} \simeq 2.3$ and 3.7 keV, respectively. From the lower panel of Fig.11, it can be observed that the time lags shift from the negative side in Case A (where $\gamma'_{i,max} > \gamma'_{eq}$) to the positive side in Case B (where $\gamma'_{i,max} < \gamma'_{eq}$). In Case A, the time lag measured by the CCF centroid is $\tau_{c,A} = -16.3$ minutes, approximately half of the maximum lags observed in the Fourier domain. In Case B, the CCF lag is $\tau_{c,B} \simeq 32.9$ minutes, approximately equal to the Fourier time lag at low frequencies, where the dependence of lag on frequency is very weak.

It should be pointed out that the power-law index of the injection electron spectra also plays an important role in determining the time lags measured between two LCs. This is due to the fact that the injected electron spectra, which are harder than the equilibrium distribution established by a balance between the various competing processes, can shelter out the spectral hardening caused by acceleration. Thus, as $\gamma'_{i,max}$ gradually tends toward γ'_{eq} the amount of time lag $|\tau|$ in Case B should approach zero, and then an increase in $|\tau|$ can be expected as the injected electron spectra gradually become softer.

Moreover, the choice of ν_{pk} (or D_0) is important for determining $|\tau|$ in the cooling-dominated case, except for B' and δ_D (see Eq.1). In the test, we select a smaller $h\nu_{pk} \simeq 1$ keV, while only q'_0 and p are adjusted to produce a similar SED as Case A. The resulting SED and time lags are displayed in Fig.11, denoted by blue

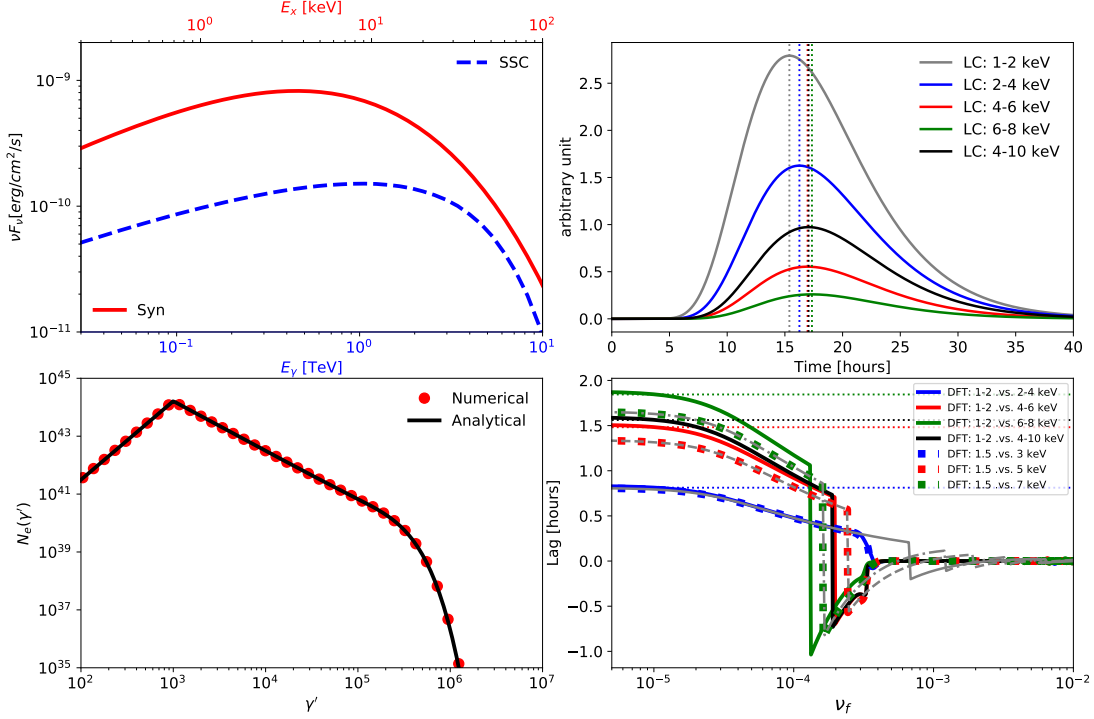


Figure 10. Comparison between analytical and numerical solutions. Upper left: the theoretical synchrotron and SSC spectrum emitted by the equilibrium EED; Lower left: the analytical and numerical solutions of the emitting EED; Upper right: the integrated LCs at five bandpasses; Lower right: the Fourier frequency-dependent time lags.

Table 6. Input model parameters and derived quantities for the studies of time lags.

Model	δ_D	B'	R'	$\nu_{pk}(E_{pk})$	q'_0	$\gamma'_{i,min}$	$\gamma'_{i,max}$	p	η_{esc}	t'_{acc}	D_0	U'_e/U'_B	τ_c
		G	10^{15} cm	10^{17} Hz (keV)	s^{-1}	10^3	10^5			R'/c	$10^{-6} s^{-1}$		min
(1)	(2)	(3)	(4)	(5)	(6)	(7)	(8)	(9)	(10)	(11)	(12)	(13)	(14)
Case A	37	0.15	2.5	5.5(2.27)	5.10×10^{45}	2.0	5.0	2.23	1.26	2.49	1.20	11.9	-16.3
Case B	35			9.0(3.72)	0.21×10^{45}		1.0	1.85		1.90	1.58	12.1	32.9
Case C				2.5(1.03)	0.12×10^{45}			1.88		3.70	0.81	10.3	-19.7
Case A1	35			5.8(2.40)	6.16×10^{45}		5.5	2.28	1.00	2.36	1.27	12.9	1.1
Case A2	38			4.0(1.65)	2.12×10^{45}		4.5	2.11	1.69	2.96	1.01	11.2	-12.6
Case A3	40				2.85×10^{45}	0.8		2.22		2.59	1.16	11.4	-19.1
Case A4	33			4.5(1.86)	1.55×10^{46}	10		2.26		2.60	1.15	11.8	-13.5
Case A5		0.08	4.5		5.18×10^{45}		6.8			3.56	0.47	20.2	-43.5
Case A6	52	0.08			1.34×10^{45}		5.8			7.59	0.39	34.6	-33.1
Case B1	33			8.3(3.43)	0.38×10^{45}			1.95	1.00	1.92	1.56	13.0	39.4
Case B2	36		2.3	11.0(4.55)	3.73×10^{43}			1.65	1.54	1.89	1.72	13.2	26.4
Case B3	36			9.3(3.85)	0.16×10^{45}	0.8				1.89	1.58	11.9	31.8
Case B4	33			8.7(3.60)	0.35×10^{45}	10				1.87	1.60	11.5	34.2
Case B5		0.08	4.7	9.5(3.93)	0.23×10^{45}					2.52	0.63	18.9	89.1
Case B6	50	0.08		9.5(3.93)	5.26×10^{43}					5.77	0.53	33.4	71.1

NOTE—Column(2-13): same as Tab.3. Column(14): The time lag measured by the CCF centroid.

solid lines. It is referred to as Case C. In the case, the amount of the time lag $|\tau_{f,C}|$ in the Fourier domain increases with decreasing of the frequencies, ended by a weakly frequency-dependent spectrum that is similar with that in the acceleration-dominated case. Meanwhile, a slightly larger $|\tau_{c,C}| = 19.7$ minutes is measured using CCF centroid, although it does not significantly differ from $|\tau_{c,A}| = 16.3$ in Case A. This is because the decrease in ν_{pk} results in the dominance of cooling processes over the electrons responsible for the 1 – 2 keV X-ray emission, which primarily undergo acceleration in Case A (where $h\nu_{pk} \simeq 2.3$ keV).

Given the values of B' and δ_D in Case A, Eq.1 yields $|\tau_A| \simeq 67.7$ minutes, which is about 3 – 4 times larger than $|\tau_{c,A/C}|$, even about 1.5 times larger than the low-frequency Fourier time lags in Case C. On the other hand, substituting the values of t'_{acc} and δ_D into Eq.6, one can find $\tau_B \simeq 120$ minutes in Case B. The result is about four times larger than the CCF and the low-frequency Fourier time lags. These imply that the relevant physical quantities inferred using the simple relationships may be significantly overestimated.

In addition, it should be pointed out that the oscillatory behavior at high frequencies is quite complex, and it is difficult to understand based on the exact analytical solution given by Eq.D11. Our extensive numerical experiments showed that the features may be related to various characteristic timescales associated with various physical processes involved. However, the features appear at frequencies beyond our interesting frequency range, and we found no significant effects on the profiles of the Fourier time lag at low frequencies, as well as on the resulting CCF lag.

Fig.12 is designed to examine the effects of variations in the parameters η_{esc} and $\gamma'_{i,min}$ that are fixed in the previous modeling due to the absence of effective constraints from the observed SED. For the cooling-dominated case, we have tested two different values of $\eta_{esc} = 1.0$ (Case A1) and 1.69 (Case A2), while $\eta_{esc} = 1.0$ (Case B1) and 1.54 (Case B2) are used for the acceleration-dominated case. For the minimum injected Lorentz factor $\gamma'_{i,min}$, we explored the effects of the associated time lags with two different values of $\gamma'_{i,min} = 8 \times 10^2$ (Case A3 and B3) and 10^4 (Case A4 and B4). To minimize the variations in both X-ray and TeV γ -ray spectra as much as possible, several other physical quantities are varied around Case A (or B).

As can be seen from Tab.6, the presence of a small hard CCF lag $\tau_{c,A1}$ in Case A1 cannot be attributed to a minor decrease in δ_D due to $|\tau| \propto 1/\sqrt{\delta_D}$, while only a minor increase in δ_D is not enough to produce the smaller soft CCF lag of $\tau_{c,A2} \simeq 0.8\tau_{c,A}$ in Case A2.

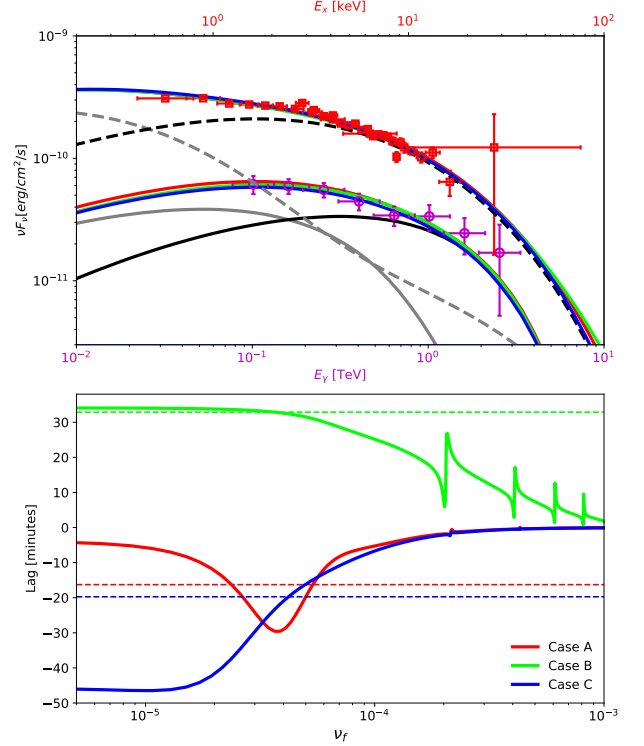


Figure 11. The theoretical SEDs (upper) and time lags (lower) resulting from variations in ν_{pk} and $\gamma'_{i,max}$. In the lower panel, the Fourier time lag profiles for Case A, B and C are denoted by the red, green and blue solid lines, respectively. The horizontal red, green and blue dashed lines mark the CCF lags for Case A, B and C, respectively. In the upper panel, the empty red squares and magenta circles represent the simultaneous X-ray and TeV γ -ray data on 2010 March 22 (MJD 55277), reported in [Aleksić et al. \(2015\)](#), respectively. The gray dashed and solid lines denote the synchrotron and SSC spectrum from the stationary zone, respectively. The synchrotron and SSC spectrum from the non-stationary zone for Case A are denoted by the black dashed and solid lines, respectively. The red, green and blue solid lines are the SEDs from non-stationary zone corresponding to Case A, B and C, superimposed with the SED from the (quasi-)stationary zone.

Similarly, the measured CCF lags of $\tau_{c,A3} \simeq 1.2\tau_{c,A}$ in Case A3 is inconsistent with the expected smaller soft lags arising from an increase in δ_D , and the measured CCF lags of $\tau_{c,A4} \simeq 0.8\tau_{c,A}$ conflict with the expected larger soft lags caused by a decrease in δ_D . In fact, the discrepancies are primarily related to small changes in D_0 and $\gamma'_{i,max}$. More detailed information of the variations in the physical quantities can be observed in the frequency-dependent spectra presented in Fig. 11.

For the acceleration-dominated cases where $\tau \propto 1/\sqrt{\nu_{pk}\delta_D}$, our results show that $\tau_{c,B1/B2}/\tau_{c,B} \simeq$

1.2(0.8) is comparable with $\sqrt{[\nu_{\text{pk}}\delta_{\text{D}}]_{\text{B}}/[\nu_{\text{pk}}\delta_{\text{D}}]_{\text{B1/B2}}} \simeq 1.1(0.9)$. The small discrepancies are due to small adjustments in p . For Case B3 and B4, we find that $\tau_{\text{c,B3/B4}}/\tau_{\text{c,B}} \simeq \sqrt{[\nu_{\text{pk}}\delta_{\text{D}}]_{\text{B}}/[\nu_{\text{pk}}\delta_{\text{D}}]_{\text{B3/B4}}} \simeq 0.97(1.05)$. Moreover, the measured CCF lags are very close to the low-frequency Fourier time lags.

It is clear that the time lags resulting from our model exhibit a substantial dependence on the specific choice of η_{esc} , accompanied by small variations in the relevant

physical quantities. These suggest that a modest adjustment to η_{esc} will not significantly affect our results inferred from the modeling of the measured time lags. On the other hand, we find that changes in the theoretical time lags and the relevant physical quantities are very small, even though $\gamma'_{\text{i,min}}$ varies by an order of magnitude. This can be easily understood since the X-rays are predominately emitted by the highest energy electrons.

REFERENCES

- Abdo, A. A., Ackermann, M., Agudo, I., et al. 2010, *ApJ*, 716, 30, doi: [10.1088/0004-637X/716/1/30](https://doi.org/10.1088/0004-637X/716/1/30)
- Abdo, A. A., Ackermann, M., Ajello, M., et al. 2011, *ApJ*, 736, 131, doi: [10.1088/0004-637X/736/2/131](https://doi.org/10.1088/0004-637X/736/2/131)
- Abeysekara, A. U., Archambault, S., Archer, A., et al. 2017a, *ApJ*, 834, 2, doi: [10.3847/1538-4357/834/1/2](https://doi.org/10.3847/1538-4357/834/1/2)
- . 2017b, *ApJ*, 836, 205, doi: [10.3847/1538-4357/836/2/205](https://doi.org/10.3847/1538-4357/836/2/205)
- Abeysekara, A. U., Benbow, W., Bird, R., et al. 2020, *ApJ*, 890, 97, doi: [10.3847/1538-4357/ab6612](https://doi.org/10.3847/1538-4357/ab6612)
- Achterberg, A., Gallant, Y. A., Kirk, J. G., & Guthmann, A. W. 2001, *MNRAS*, 328, 393, doi: [10.1046/j.1365-8711.2001.04851.x](https://doi.org/10.1046/j.1365-8711.2001.04851.x)
- Aguilar-Ruiz, E., Fraija, N., Galván-Gómez, A., & Benítez, E. 2022, *MNRAS*, 512, 1557, doi: [10.1093/mnras/stac591](https://doi.org/10.1093/mnras/stac591)
- Aharonian, F., Akhperjanian, A. G., Anton, G., et al. 2009, *A&A*, 502, 749, doi: [10.1051/0004-6361/200912128](https://doi.org/10.1051/0004-6361/200912128)
- Aleksić, J., Alvarez, E. A., Antonelli, L. A., et al. 2012, *A&A*, 542, A100, doi: [10.1051/0004-6361/201117442](https://doi.org/10.1051/0004-6361/201117442)
- Aleksić, J., Ansoldi, S., Antonelli, L. A., et al. 2015, *A&A*, 578, A22, doi: [10.1051/0004-6361/201424811](https://doi.org/10.1051/0004-6361/201424811)
- Baloković, M., Paneque, D., Madejski, G., et al. 2016, *ApJ*, 819, 156, doi: [10.3847/0004-637X/819/2/156](https://doi.org/10.3847/0004-637X/819/2/156)
- Banerjee, B., Joshi, M., Majumdar, P., et al. 2019, *MNRAS*, 487, 845, doi: [10.1093/mnras/stz1292](https://doi.org/10.1093/mnras/stz1292)
- Baring, M. G., Böttcher, M., & Summerlin, E. J. 2017, *MNRAS*, 464, 4875, doi: [10.1093/mnras/stw2344](https://doi.org/10.1093/mnras/stw2344)
- Becker, P. A., Le, T., & Dermer, C. D. 2006, *ApJ*, 647, 539, doi: [10.1086/505319](https://doi.org/10.1086/505319)
- Bednarz, J., & Ostrowski, M. 1998, *PhRvL*, 80, 3911, doi: [10.1103/PhysRevLett.80.3911](https://doi.org/10.1103/PhysRevLett.80.3911)
- Begelman, M. C., & Kirk, J. G. 1990, *ApJ*, 353, 66, doi: [10.1086/168590](https://doi.org/10.1086/168590)
- Bell, A. R. 1978, *MNRAS*, 182, 147, doi: [10.1093/mnras/182.2.147](https://doi.org/10.1093/mnras/182.2.147)
- Blandford, R. D., & Königl, A. 1979, *ApJ*, 232, 34, doi: [10.1086/157262](https://doi.org/10.1086/157262)
- Bloom, S. D., & Marscher, A. P. 1996, *ApJ*, 461, 657, doi: [10.1086/177092](https://doi.org/10.1086/177092)
- Böttcher, M., & Baring, M. G. 2019, *ApJ*, 887, 133, doi: [10.3847/1538-4357/ab552a](https://doi.org/10.3847/1538-4357/ab552a)
- Böttcher, M., & Chiang, J. 2002, *ApJ*, 581, 127, doi: [10.1086/344155](https://doi.org/10.1086/344155)
- Böttcher, M., & Dermer, C. D. 2010, *ApJ*, 711, 445, doi: [10.1088/0004-637X/711/1/445](https://doi.org/10.1088/0004-637X/711/1/445)
- Boula, S., & Mastichiadis, A. 2022, *A&A*, 657, A20, doi: [10.1051/0004-6361/202142126](https://doi.org/10.1051/0004-6361/202142126)
- Brinkmann, W., Papadakis, I. E., den Herder, J. W. A., & Haberl, F. 2003, *A&A*, 402, 929, doi: [10.1051/0004-6361:20030264](https://doi.org/10.1051/0004-6361:20030264)
- Brinkmann, W., Papadakis, I. E., Raeth, C., Mimica, P., & Haberl, F. 2005, *A&A*, 443, 397, doi: [10.1051/0004-6361:20052767](https://doi.org/10.1051/0004-6361:20052767)
- Cerutti, B., Uzdensky, D. A., & Begelman, M. C. 2012, *ApJ*, 746, 148, doi: [10.1088/0004-637X/746/2/148](https://doi.org/10.1088/0004-637X/746/2/148)
- Chandra, S., Boettcher, M., Goswami, P., et al. 2021, *ApJ*, 918, 67, doi: [10.3847/1538-4357/ac01d1](https://doi.org/10.3847/1538-4357/ac01d1)
- Chiaberge, M., & Ghisellini, G. 1999, *MNRAS*, 306, 551, doi: [10.1046/j.1365-8711.1999.02538.x](https://doi.org/10.1046/j.1365-8711.1999.02538.x)
- Crumley, P., Caprioli, D., Markoff, S., & Spitkovsky, A. 2019, *MNRAS*, 485, 5105, doi: [10.1093/mnras/stz232](https://doi.org/10.1093/mnras/stz232)
- Crusius, A., & Schlickeiser, R. 1986, *A&A*, 164, L16
- Das, S., & Chatterjee, R. 2023, *MNRAS*, 524, 3797, doi: [10.1093/mnras/stad2131](https://doi.org/10.1093/mnras/stad2131)
- de Marco, B., Ponti, G., Uttley, P., et al. 2011, *MNRAS*, 417, L98, doi: [10.1111/j.1745-3933.2011.01129.x](https://doi.org/10.1111/j.1745-3933.2011.01129.x)
- Deng, X.-C., Hu, W., Lu, F.-W., & Dai, B.-Z. 2021, *MNRAS*, 504, 878, doi: [10.1093/mnras/stab919](https://doi.org/10.1093/mnras/stab919)
- Dermer, C. D., Finke, J. D., Krug, H., & Böttcher, M. 2009, *ApJ*, 692, 32, doi: [10.1088/0004-637X/692/1/32](https://doi.org/10.1088/0004-637X/692/1/32)
- Devanand, P. U., Gupta, A. C., Jithesh, V., & Wiita, P. J. 2022, *ApJ*, 939, 80, doi: [10.3847/1538-4357/ac9064](https://doi.org/10.3847/1538-4357/ac9064)
- Dhiman, V., Gupta, A. C., Gaur, H., & Wiita, P. J. 2021, *MNRAS*, 506, 1198, doi: [10.1093/mnras/stab1743](https://doi.org/10.1093/mnras/stab1743)

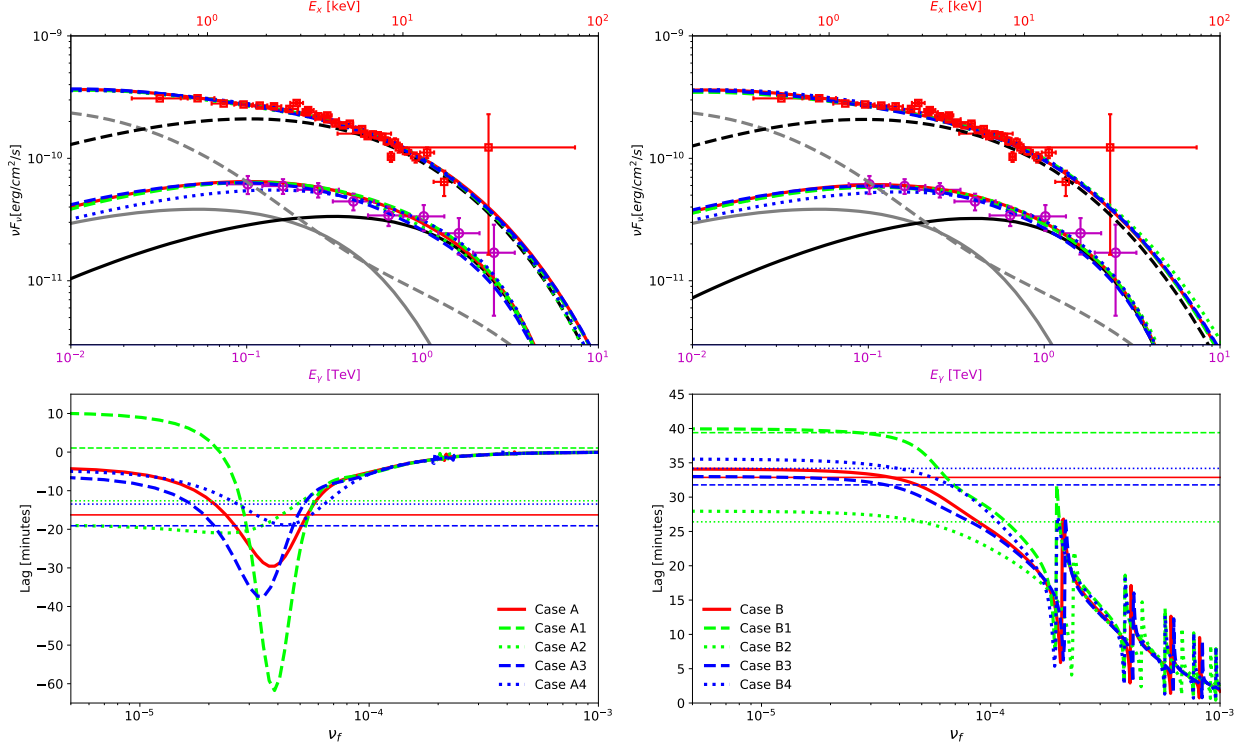


Figure 12. The theoretical SEDs (upper) and time lags (lower) resulting from variations in $\gamma'_{i,\min}$ and η_{esc} . In the lower panels, the Fourier time lag profiles for different cases are indicated in the legend, and the corresponding CCF lags are marked with the horizontal line styles. In the upper panels, the observed data points and theoretical SED from the (quasi-)stationary zone are same as those in Fig.11. The synchrotron and SSC spectrum from the non-stationary zone for Case A (left) and B (right) are denoted by the black dashed and solid lines, respectively. The SEDs from non-stationary zones are denoted by line styles that are the same as those in the lower panels, superimposed with the SED from the (quasi-)stationary zone.

Di Gesu, L., Marshall, H. L., Ehlert, S. R., et al. 2023, *Nature Astronomy*, 7, 1245, doi: [10.1038/s41550-023-02032-7](https://doi.org/10.1038/s41550-023-02032-7)

Diltz, C., & Böttcher, M. 2014, *Journal of High Energy Astrophysics*, 1, 63, doi: [10.1016/j.jheap.2014.04.001](https://doi.org/10.1016/j.jheap.2014.04.001)

—. 2016, *ApJ*, 826, 54, doi: [10.3847/0004-637X/826/1/54](https://doi.org/10.3847/0004-637X/826/1/54)

Diltz, C., Böttcher, M., & Fossati, G. 2015, *ApJ*, 802, 133, doi: [10.1088/0004-637X/802/2/133](https://doi.org/10.1088/0004-637X/802/2/133)

Dmytriiev, A., Sol, H., & Zech, A. 2021, *MNRAS*, 505, 2712, doi: [10.1093/mnras/stab1445](https://doi.org/10.1093/mnras/stab1445)

Drury, L. O. 1983, *Reports on Progress in Physics*, 46, 973, doi: [10.1088/0034-4885/46/8/002](https://doi.org/10.1088/0034-4885/46/8/002)

Ellison, D. C., & Double, G. P. 2004, *Astroparticle Physics*, 22, 323, doi: [10.1016/j.astropartphys.2004.08.005](https://doi.org/10.1016/j.astropartphys.2004.08.005)

Emmanoulopoulos, D., McHardy, I. M., & Papadakis, I. E. 2013, *MNRAS*, 433, 907, doi: [10.1093/mnras/stt764](https://doi.org/10.1093/mnras/stt764)

Fan, J. H., Yang, J. H., Liu, Y., et al. 2016, *ApJS*, 226, 20, doi: [10.3847/0067-0049/226/2/20](https://doi.org/10.3847/0067-0049/226/2/20)

Ferrero, E., Wagner, S. J., Emmanoulopoulos, D., & Ostorero, L. 2006, *A&A*, 457, 133, doi: [10.1051/0004-6361:20065317](https://doi.org/10.1051/0004-6361:20065317)

Finke, J. D., & Becker, P. A. 2014, *ApJ*, 791, 21, doi: [10.1088/0004-637X/791/1/21](https://doi.org/10.1088/0004-637X/791/1/21)

—. 2015, *ApJ*, 809, 85, doi: [10.1088/0004-637X/809/1/85](https://doi.org/10.1088/0004-637X/809/1/85)

Finke, J. D., Dermer, C. D., & Böttcher, M. 2008, *ApJ*, 686, 181, doi: [10.1086/590900](https://doi.org/10.1086/590900)

Foreman-Mackey, D., Hogg, D. W., Lang, D., & Goodman, J. 2013, *PASP*, 125, 306, doi: [10.1086/670067](https://doi.org/10.1086/670067)

Fossati, G., Maraschi, L., Celotti, A., Comastri, A., & Ghisellini, G. 1998, *MNRAS*, 299, 433, doi: [10.1046/j.1365-8711.1998.01828.x](https://doi.org/10.1046/j.1365-8711.1998.01828.x)

Fossati, G., Celotti, A., Chiaberge, M., et al. 2000a, *ApJ*, 541, 153, doi: [10.1086/309422](https://doi.org/10.1086/309422)

—. 2000b, *ApJ*, 541, 166, doi: [10.1086/309430](https://doi.org/10.1086/309430)

Fossati, G., Buckley, J. H., Bond, I. H., et al. 2008, *ApJ*, 677, 906, doi: [10.1086/527311](https://doi.org/10.1086/527311)

Giannios, D. 2013, *MNRAS*, 431, 355, doi: [10.1093/mnras/stt167](https://doi.org/10.1093/mnras/stt167)

Giannios, D., & Spruit, H. C. 2006, *A&A*, 450, 887, doi: [10.1051/0004-6361:20054107](https://doi.org/10.1051/0004-6361:20054107)

Giannios, D., Uzdensky, D. A., & Begelman, M. C. 2009, *MNRAS*, 395, L29, doi: [10.1111/j.1745-3933.2009.00635.x](https://doi.org/10.1111/j.1745-3933.2009.00635.x)

- Gokus, A., Wilms, J., Kadler, M., et al. 2024, *MNRAS*, 529, 1450, doi: [10.1093/mnras/stae643](https://doi.org/10.1093/mnras/stae643)
- Guo, F., Li, H., Daughton, W., & Liu, Y.-H. 2014, *PhRvL*, 113, 155005, doi: [10.1103/PhysRevLett.113.155005](https://doi.org/10.1103/PhysRevLett.113.155005)
- Gupta, A. C. 2020, *Galaxies*, 8, 64, doi: [10.3390/galaxies8030064](https://doi.org/10.3390/galaxies8030064)
- Hervet, O., Williams, D. A., Falcone, A. D., & Kaur, A. 2019, *ApJ*, 877, 26, doi: [10.3847/1538-4357/ab1906](https://doi.org/10.3847/1538-4357/ab1906)
- Hu, W., & Yan, D. 2021, *MNRAS*, 508, 4038, doi: [10.1093/mnras/stab2442](https://doi.org/10.1093/mnras/stab2442)
- Hu, W., Yan, D.-H., & Hu, Q.-L. 2023, *ApJ*, 948, 82, doi: [10.3847/1538-4357/acce2e](https://doi.org/10.3847/1538-4357/acce2e)
- Inoue, Y., & Tanaka, Y. T. 2016, *ApJ*, 828, 13, doi: [10.3847/0004-637X/828/1/13](https://doi.org/10.3847/0004-637X/828/1/13)
- Jansen, F., Lumb, D., Altieri, B., et al. 2001, *A&A*, 365, L1, doi: [10.1051/0004-6361:20000036](https://doi.org/10.1051/0004-6361:20000036)
- Jones, F. C. 1968, *Physical Review*, 167, 1159, doi: [10.1103/PhysRev.167.1159](https://doi.org/10.1103/PhysRev.167.1159)
- Katarzyński, K., Ghisellini, G., Mastichiadis, A., Tavecchio, F., & Maraschi, L. 2006, *A&A*, 453, 47, doi: [10.1051/0004-6361:20054176](https://doi.org/10.1051/0004-6361:20054176)
- Kirk, J. G., Duffy, P., & Gallant, Y. A. 1996, *A&A*, 314, 1010, doi: [10.48550/arXiv.astro-ph/9604056](https://doi.org/10.48550/arXiv.astro-ph/9604056)
- Kirk, J. G., Guthmann, A. W., Gallant, Y. A., & Achterberg, A. 2000, *ApJ*, 542, 235, doi: [10.1086/309533](https://doi.org/10.1086/309533)
- Kirk, J. G., & Heavens, A. F. 1989, *MNRAS*, 239, 995, doi: [10.1093/mnras/239.3.995](https://doi.org/10.1093/mnras/239.3.995)
- Kirk, J. G., Rieger, F. M., & Mastichiadis, A. 1998, *A&A*, 333, 452, doi: [10.48550/arXiv.astro-ph/9801265](https://doi.org/10.48550/arXiv.astro-ph/9801265)
- Konigl, A. 1981, *ApJ*, 243, 700, doi: [10.1086/158638](https://doi.org/10.1086/158638)
- Kroon, J. J., & Becker, P. A. 2014, *ApJL*, 785, L34, doi: [10.1088/2041-8205/785/2/L34](https://doi.org/10.1088/2041-8205/785/2/L34)
- Kusunose, M., Takahara, F., & Li, H. 2000, *ApJ*, 536, 299, doi: [10.1086/308928](https://doi.org/10.1086/308928)
- Larionov, V. M., Jorstad, S. G., Marscher, A. P., et al. 2013, *ApJ*, 768, 40, doi: [10.1088/0004-637X/768/1/40](https://doi.org/10.1088/0004-637X/768/1/40)
- Lewis, T. R., Becker, P. A., & Finke, J. D. 2016, *ApJ*, 824, 108, doi: [10.3847/0004-637X/824/2/108](https://doi.org/10.3847/0004-637X/824/2/108)
- Lewis, T. R., Finke, J. D., & Becker, P. A. 2018, *ApJ*, 853, 6, doi: [10.3847/1538-4357/aaa19a](https://doi.org/10.3847/1538-4357/aaa19a)
- Li, H., & Kusunose, M. 2000, *ApJ*, 536, 729, doi: [10.1086/308960](https://doi.org/10.1086/308960)
- Liu, R.-Y., Xue, R., Wang, Z.-R., Tan, H.-B., & Böttcher, M. 2023, *MNRAS*, 526, 5054, doi: [10.1093/mnras/stad2911](https://doi.org/10.1093/mnras/stad2911)
- MacDonald, N. R., Marscher, A. P., Jorstad, S. G., & Joshi, M. 2015, *ApJ*, 804, 111, doi: [10.1088/0004-637X/804/2/111](https://doi.org/10.1088/0004-637X/804/2/111)
- MAGIC Collaboration, Acciari, V. A., Ansoldi, S., et al. 2021, *A&A*, 655, A89, doi: [10.1051/0004-6361/202141004](https://doi.org/10.1051/0004-6361/202141004)
- Mankuzhiyil, N., Ansoldi, S., Persic, M., & Tavecchio, F. 2011, *ApJ*, 733, 14, doi: [10.1088/0004-637X/733/1/14](https://doi.org/10.1088/0004-637X/733/1/14)
- Marscher, A. P., & Gear, W. K. 1985, *ApJ*, 298, 114, doi: [10.1086/163592](https://doi.org/10.1086/163592)
- Mastichiadis, A., & Kirk, J. G. 1997, *A&A*, 320, 19, doi: [10.48550/arXiv.astro-ph/9610058](https://doi.org/10.48550/arXiv.astro-ph/9610058)
- Moderski, R., Sikora, M., Coppi, P. S., & Aharonian, F. 2005, *Monthly Notices of the Royal Astronomical Society*, 363, 954, doi: [10.1111/j.1365-2966.2005.09494.x](https://doi.org/10.1111/j.1365-2966.2005.09494.x)
- Nalewajko, K., & Begelman, M. C. 2012, *MNRAS*, 427, 2480, doi: [10.1111/j.1365-2966.2012.22117.x](https://doi.org/10.1111/j.1365-2966.2012.22117.x)
- Ng, C., Díaz Trigo, M., Cadolle Bel, M., & Migliari, S. 2010, *A&A*, 522, A96, doi: [10.1051/0004-6361/200913575](https://doi.org/10.1051/0004-6361/200913575)
- Niemiec, J., & Ostrowski, M. 2004, *ApJ*, 610, 851, doi: [10.1086/421730](https://doi.org/10.1086/421730)
- Noel, A. P., Gaur, H., Gupta, A. C., et al. 2022, *ApJS*, 262, 4, doi: [10.3847/1538-4365/ac7799](https://doi.org/10.3847/1538-4365/ac7799)
- Peterson, B. M., Wanders, I., Horne, K., et al. 1998, *PASP*, 110, 660, doi: [10.1086/316177](https://doi.org/10.1086/316177)
- Petropoulou, M., Giannios, D., & Sironi, L. 2016, *MNRAS*, 462, 3325, doi: [10.1093/mnras/stw1832](https://doi.org/10.1093/mnras/stw1832)
- Petropoulou, M., Sironi, L., Spitkovsky, A., & Giannios, D. 2019, *ApJ*, 880, 37, doi: [10.3847/1538-4357/ab287a](https://doi.org/10.3847/1538-4357/ab287a)
- Piran, T. 1999, *PhR*, 314, 575, doi: [10.1016/S0370-1573\(98\)00127-6](https://doi.org/10.1016/S0370-1573(98)00127-6)
- Prince, R., Gupta, N., & Nalewajko, K. 2019, *ApJ*, 883, 137, doi: [10.3847/1538-4357/ab3afa](https://doi.org/10.3847/1538-4357/ab3afa)
- Rani, B., Krichbaum, T. P., Fuhrmann, L., et al. 2013, *A&A*, 552, A11, doi: [10.1051/0004-6361/201321058](https://doi.org/10.1051/0004-6361/201321058)
- Ravasio, M., Tagliaferri, G., Ghisellini, G., & Tavecchio, F. 2004, *A&A*, 424, 841, doi: [10.1051/0004-6361:20034545](https://doi.org/10.1051/0004-6361:20034545)
- Rybicki, G. B., & Lightman, A. P. 1979, *Radiative processes in astrophysics*
- Schlickeiser, R. 1984, *A&A*, 136, 227
- . 1989, *ApJ*, 336, 243, doi: [10.1086/167009](https://doi.org/10.1086/167009)
- Shukla, A., Chitnis, V. R., Vishwanath, P. R., et al. 2012, *A&A*, 541, A140, doi: [10.1051/0004-6361/201118569](https://doi.org/10.1051/0004-6361/201118569)
- Sinha, A., Shukla, A., Saha, L., et al. 2016, *A&A*, 591, A83, doi: [10.1051/0004-6361/201628152](https://doi.org/10.1051/0004-6361/201628152)
- Sironi, L., Petropoulou, M., & Giannios, D. 2015, *MNRAS*, 450, 183, doi: [10.1093/mnras/stv641](https://doi.org/10.1093/mnras/stv641)
- Sironi, L., & Spitkovsky, A. 2009, *ApJL*, 707, L92, doi: [10.1088/0004-637X/707/1/L92](https://doi.org/10.1088/0004-637X/707/1/L92)
- . 2014, *ApJL*, 783, L21, doi: [10.1088/2041-8205/783/1/L21](https://doi.org/10.1088/2041-8205/783/1/L21)
- Sironi, L., Spitkovsky, A., & Arons, J. 2013, *ApJ*, 771, 54, doi: [10.1088/0004-637X/771/1/54](https://doi.org/10.1088/0004-637X/771/1/54)
- Spada, M., Ghisellini, G., Lazzati, D., & Celotti, A. 2001, *MNRAS*, 325, 1559, doi: [10.1046/j.1365-8711.2001.04557.x](https://doi.org/10.1046/j.1365-8711.2001.04557.x)

- Stawarz, L., & Petrosian, V. 2008, *ApJ*, 681, 1725, doi: [10.1086/588813](https://doi.org/10.1086/588813)
- Strüder, L., Briel, U., Dennerl, K., et al. 2001, *A&A*, 365, L18, doi: [10.1051/0004-6361:20000066](https://doi.org/10.1051/0004-6361:20000066)
- Summerlin, E. J., & Baring, M. G. 2012, *ApJ*, 745, 63, doi: [10.1088/0004-637X/745/1/63](https://doi.org/10.1088/0004-637X/745/1/63)
- Tammi, J., & Duffy, P. 2009, *MNRAS*, 393, 1063, doi: [10.1111/j.1365-2966.2008.14270.x](https://doi.org/10.1111/j.1365-2966.2008.14270.x)
- Tavecchio, F., Becerra-Gonzalez, J., Ghisellini, G., et al. 2011, *A&A*, 534, A86, doi: [10.1051/0004-6361/201117204](https://doi.org/10.1051/0004-6361/201117204)
- Timmer, J., & Koenig, M. 1995, *A&A*, 300, 707
- Tramacere, A., Giommi, P., Perri, M., Verrecchia, F., & Tosti, G. 2009, *A&A*, 501, 879, doi: [10.1051/0004-6361/200810865](https://doi.org/10.1051/0004-6361/200810865)
- Tramacere, A., Massaro, E., & Taylor, A. M. 2011, *ApJ*, 739, 66, doi: [10.1088/0004-637X/739/2/66](https://doi.org/10.1088/0004-637X/739/2/66)
- Tramacere, A., Massaro, F., & Cavaliere, A. 2007, *A&A*, 466, 521, doi: [10.1051/0004-6361:20066723](https://doi.org/10.1051/0004-6361:20066723)
- Urry, C. M., & Padovani, P. 1995, *PASP*, 107, 803, doi: [10.1086/133630](https://doi.org/10.1086/133630)
- Ushio, M., Stawarz, L., Takahashi, T., et al. 2010, *ApJ*, 724, 1509, doi: [10.1088/0004-637X/724/2/1509](https://doi.org/10.1088/0004-637X/724/2/1509)
- Uttley, P., Cackett, E. M., Fabian, A. C., Kara, E., & Wilkins, D. R. 2014, *A&A Rv*, 22, 72, doi: [10.1007/s00159-014-0072-0](https://doi.org/10.1007/s00159-014-0072-0)
- Vaughan, B. A., & Nowak, M. A. 1997, *ApJL*, 474, L43, doi: [10.1086/310430](https://doi.org/10.1086/310430)
- Vaughan, S. 2010, *MNRAS*, 402, 307, doi: [10.1111/j.1365-2966.2009.15868.x](https://doi.org/10.1111/j.1365-2966.2009.15868.x)
- Vaughan, S., Edelson, R., Warwick, R. S., & Uttley, P. 2003, *MNRAS*, 345, 1271, doi: [10.1046/j.1365-2966.2003.07042.x](https://doi.org/10.1046/j.1365-2966.2003.07042.x)
- Wang, Z.-R., Liu, R.-Y., Petropoulou, M., et al. 2022, *PhRvD*, 105, 023005, doi: [10.1103/PhysRevD.105.023005](https://doi.org/10.1103/PhysRevD.105.023005)
- Weidinger, M., Rügner, M., & Spanier, F. 2010, *Astrophysics and Space Sciences Transactions*, 6, 1, doi: [10.5194/astra-6-1-2010](https://doi.org/10.5194/astra-6-1-2010)
- Wiercholska, A., Zacharias, M., Jankowsky, F., Wagner, S., & H. E. S. S. Collaboration. 2019, *Galaxies*, 7, 21, doi: [10.3390/galaxies7010021](https://doi.org/10.3390/galaxies7010021)
- Xue, R., Liu, R.-Y., Petropoulou, M., et al. 2019, *ApJ*, 886, 23, doi: [10.3847/1538-4357/ab4b44](https://doi.org/10.3847/1538-4357/ab4b44)
- Yan, D., Yang, S., Zhang, P., et al. 2018, *ApJ*, 864, 164, doi: [10.3847/1538-4357/aadd01](https://doi.org/10.3847/1538-4357/aadd01)
- Zacharias, M., & Schlickeiser, R. 2013, *ApJ*, 777, 109, doi: [10.1088/0004-637X/777/2/109](https://doi.org/10.1088/0004-637X/777/2/109)
- Zhang, Y. H. 2002, *MNRAS*, 337, 609, doi: [10.1046/j.1365-8711.2002.05958.x](https://doi.org/10.1046/j.1365-8711.2002.05958.x)
- Zhang, Y. H., Treves, A., Maraschi, L., Bai, J. M., & Liu, F. K. 2006, *ApJ*, 637, 699, doi: [10.1086/498498](https://doi.org/10.1086/498498)